# Multiple sulphur and lead sources recorded in hydrothermal exhalites associated with the Lemarchant volcanogenic massive sulphide deposit, central Newfoundland, Canada

Stefanie Lode[1*], Stephen J. Piercey[1], Graham D. Layne[1], Glenn Piercey[2], and Jonathan Cloutier[1,3]

1 - Department of Earth Sciences, Memorial University, 300 Prince Philip Drive, St. John's, NL, Canada, A1B 3X5

2 - MAF-IIC SIMS Facility, Memorial University, St. John's, NL, Canada, A1B 3X5

3 - Department of Earth Sciences, University of St. Andrews, St. Andrews, Scotland, UK, KY16 9AL

*Corresponding author – slode@mun.ca, +1 709 697 9082

**Abstract**

Metalliferous sedimentary rocks (mudstones, exhalites) associated with the Cambrian precious metal-bearing Lemarchant Zn-Pb-Cu-Au-Ag-Ba volcanogenic massive sulphide (VMS) deposit, Tally Pond volcanic belt, precipitated both before and after VMS mineralization. Sulphur and Pb isotopic studies of sulphides within the Lemarchant exhalites provide insight into the sources of S and Pb in the exhalites as a function of paragenesis and evolution of the deposit, and subsequent post-depositional modification. *In situ* S isotope microanalyses of polymetallic sulphides (euhedral and framboidal pyrite, anhedral chalcopyrite, pyrrhotite, galena and euhedral arsenopyrite) by secondary ion mass spectrometry (SIMS) yielded $\delta^{34}S$ values ranging from -38.8‰ to +14.4‰, with an average of ~ -12.8‰. The $\delta^{34}S$ systematics indicate sulphur was predominantly biogenically-derived via microbial/biogenic sulphate reduction of seawater sulphate, microbial sulphide oxidation, and microbial disproportionation of intermediate S compounds. These biogenic processes are coupled and occur within layers of microbial mats consisting of different bacterial/archaeal species, i.e., sulphate reducers, sulphide oxidizers, and those that disproportionate sulphur compounds. Inorganic processes or sources (i.e., thermochemical sulphate reduction of seawater sulphate, leached or direct igneous sulphur) also contributed to the S budget in the hydrothermal exhalites, and are more pronounced in exhalites that are immediately associated with massive sulphides.

Galena Pb isotopic compositions by SIMS microanalysis suggest derivation of Pb from underlying crustal basement (felsic volcanic rocks of Sandy Brook Group), whereas less radiogenic Pb derived from juvenile sources leached from mafic volcanic rocks of

the Sandy Brook Group and/or Tally Pond group. This requires that the hydrothermal fluids interacted with juvenile and evolved crust during hydrothermal circulation, which is consistent with the existing tectonic model that suggests a formation of the Tally Pond belt volcanic rocks and associated VMS deposits in a rifted arc environment upon crustal basement of the Ediacaran age Sandy Brook Group and Crippleback Intrusive Suite. Combined S and Pb isotope data illustrate that sulphides within the deposit that are proximal to the vent, contain a higher proportion of sulphur derived from thermochemical sulphate reduction (TSR), because hydrothermal fluids are enriched in $H_2S$ derived from TSR. They also have lower radiogenic Pb contributions, than sulphides occurring distal from mineralization. Hence, the TSR S and non-radiogenic Pb composition may provide an exploration vector in exhalites associated with similar VMS environments.

**Keywords**

VMS, exhalites, sulphur and lead isotopes, TSR, BSR, BSO, disproportionation

## Introduction

Metalliferous sedimentary rocks (exhalites, mudstones) are commonly associated with volcanogenic massive sulphide (VMS) deposits (Franklin et al. 1981; Lydon 1984; Kalogeropoulos and Scott 1989; Spry et al. 2000; Peter 2003; Hannington 2014). Metalliferous sediments can pre- or post-date massive sulphide mineralization. They precipitate as hydrothermal plume fallout proximal to the hydrothermal vent, but also occur as thin layers up to several kilometres away from the vent site (Haymon and Kastner 1981; Lydon 1984; Haymon et al. 1993; Hodkinson and Cronan 1995; Binns 2004; Gurvich 2006; Hannington 2014). Iron, Zn, Pb, and Cu sulphides co-precipitate with sulphates (barite, anhydrite), and other phases (amorphous silica and Fe-oxyhydroxides), from the buoyant to neutrally-buoyant hydrothermal plume after mixing with the ambient seawater (Haymon and Kastner 1981; Campbell et al. 1984; Hodkinson and Cronan 1995; German and Von Damm 2003; Binns 2004; Dias et al. 2008; Hannington 2009; Hekinian et al. 1993). These exhalites consist of hydrothermal, seawater, and detrital components that are reflected in their sediment mineralogy, chemistry, and S and Pb isotopic compositions (Boström and Peterson 1966; Boström et al. 1969; Shanks 2001; German and Von Damm 2003; Dias et al. 2008; Shanks 2014).

Reduced S in volcanogenic massive sulphide and associated hydrothermal sedimentary rocks can be derived from various sources and processes, both inorganic and organic. Inorganic sources include: 1) thermochemical reduction of seawater sulphate (TSR); 2) magmatic contributions through leaching of sulphur from igneous rocks or direct magmatic fluid/volatile input; and/or 3) sedimentary-diagenetic sulphides (Ohmoto and Rye 1979; Ohmoto and Goldhaber 1997; Seal 2006; Shanks 2014). Hydrogen

sulphide ($H_2S$), a by-product of TSR is present in the buoyant plume when the hydrothermal fluids exit the seafloor via black smokers, but also in hot pore waters that circulate upwards through the porous sulphide mound and flanking sediments and subsequently emanate as diffuse hydrothermal flow into the ambient seawater column (Von Damm 1990; Gundersen et al. 1992; Elsgaard et al. 1994; Hannington et al. 1995; German and Von Damm 2003; Hannington 2014). Additionally, $H_2S$ can be incorporated into the hydrothermal fluids by direct degassing of magmas (Hannington et al. 1999). In some massive sulphide deposits, and associated metalliferous mudstones, biogenically-derived sulphide plays a substantial role in their sulphur budget - with organic sulphur derived from the biogenic/microbial (bacterial and archaeal) reduction of seawater sulphate (BSR), and the microbial disproportionation of sulphur intermediates, with an intermediate step of biogenic sulphide oxidation (Harrison and Thode 1958; Elsgaard et al. 1994; Canfield 2001b; Habicht and Canfield 2001; Shanks 2001; Seal 2006; Shanks 2014). Microbial sulphate reduction, coupled with microbial disproportionation of sulphur intermediate compounds, is associated with large $\Delta^{34}S_{sulphate\text{-}H_2S}$ fractionation, which results in sedimentary, and massive, sulphides with strong $^{34}S$-depletion (Bak and Pfennig 1987; Jørgensen 1990; Jørgensen et al. 1992; Canfield 2001b; Habicht and Canfield 2001; Habicht and Canfield 1997). The mineral specific S isotope systematics of polymetallic sulphides in metalliferous exhalites thus provide the opportunity to evaluate sulphur sources in the exhalites, and allow delineation of sulphur sources as a function of paragenesis and the multi-stage evolution of the underlying deposit.

Similarly, Pb isotopes provide insight into the source of metals within massive sulphides and other ore deposits and their lithological provenance (Swinden and Thorpe

1984; Zartman and Doe 1981;  Tosdal et al. 1999; Ayuso et al. 2003). In VMS deposits, Pb is predominantly leached from basement rocks, which can have varying Pb isotope signatures when derived from different reservoirs (Franklin and Thorpe 1982; Swinden and Thorpe 1984; Tosdal et al. 1999; Ayuso et al. 2003). Determining Pb isotopic ratios in galena hosted in the Lemarchant metalliferous exhalites therefore provides a possibility to identify sources of Pb that contributed to the Lemarchant exhalites.

The Cambrian precious metal-bearing Lemarchant Pb-Zn-Cu VMS deposit provides an ideal location to study the S and Pb sources in metalliferous mudstones associated with massive sulphide mineralization. In this deposit metalliferous mudstones are located immediately atop massive sulphides and also at a considerable distance from mineralization. A hydrothermal origin for these metalliferous mudstones has been shown (Lode et al. 2015), and these mudstones can be considered as exhalites (Ridler 1971; Peter and Goodfellow 2003; Galley et al. 2007). Furthermore, the Lemarchant exhalites have exquisite textural and paragenetic preservation, thus providing an opportunity to evaluate changing sources of S and Pb in both space, and as a function of deposit evolution. These data also contribute to understanding the tectonic environment and paleoceanographic environment of formation for the Lemarchant deposit. Finally, the data presented herein have implications for utilizing S and Pb in hydrothermal sedimentary rocks as a potential vector for VMS deposits in similar geological environments.

**Regional and deposit geology**

The Zn-Pb-Cu-Ba-Au-Ag-bearing Lemarchant deposit is hosted within the Central Mobile Belt, Newfoundland, part of the Cambrian (~515 Ma) to Permian (~275

Ma) Appalachian mountain belt (Fig. 1a; Williams 1979; Swinden 1988; Swinden 1991; Squires and Moore 2004; Franklin et al. 2005; Piercey 2007; Rogers et al. 2007; Copeland et al. 2009; McNicoll et al. 2010; van Staal and Barr 2011). The Central Mobile Belt hosts numerous VMS deposits and was only moderately affected by metamorphism (lower greenschist-facies) and deformation during the three Late Cambrian to Late Ordovician (495-450 Ma) Taconic orogenies and the Early Silurian (440-423 Ma) Salinic Orogeny (Swinden 1991; Squires and Moore 2004; van Staal and Barr 2011). The internal stratigraphic and textural relationships are well preserved, both regionally, and within the VMS deposits (Hinchey and McNicoll 2009; Zagorevski et al. 2010; van Staal and Barr 2011; Piercey et al. 2014).

The Newfoundland Appalachians are divided into four tectonostratigraphic zones: Humber, Dunnage, Gander and Avalon (Fig. 1a). These zones result from, and were affected by, the successive accretion of three micro-continental blocks and related interoceanic arcs and backarcs during the Early Paleozoic to Middle Paleozoic (Swinden 1991; Rogers et al. 2007; van Staal 2007; Zagorevski et al. 2010; van Staal and Barr 2011). These ribbon-shaped micro-continental blocks were located on the leading edges of Gondwana and Laurentia, forming peri-Gondwanan and peri-Laurentian terranes (Rogers et al. 2007; Zagorevski et al. 2010; van Staal and Barr 2011). The Dunnage Zone (~Central Mobile Belt; Williams 1979; Williams et al. 1988; Swinden 1991; Squires and Moore 2004) has been subdivided into the peri-Laurentian Notre Dame and the peri-Gondwanan Exploits subzones (Swinden 1988; Swinden 1991; Pollock and Wilton 2001)(Fig. 1a). The Exploits Subzone is comprised of Cambrian-Ordovician volcanic and sedimentary rocks (Dunning et al. 1991; Rogers et al. 2007; van Staal and Barr 2011;

McNicoll et al. 2010) and includes the Victoria Lake Supergroup. The Lemarchant deposit and the Duck Pond and Boundary mines are located within the Tally Pond group, one of the six tectonic assemblages within the Victoria Lake Supergroup that yield U-Pb zircon ages ranging from ~513 to 453 Ma (Dunning et al. 1987; Dunning et al. 1991; Evans and Kean 2002; Rogers et al. 2007; Zagorevski et al. 2007; McNicoll et al. 2010; Zagorevski et al. 2010; Piercey et al. 2014). The Tally Pond group (~513-509 Ma) is further divided into the Bindons Pond and the Lake Ambrose formations (Fig. 1b) and is interpreted to have been formed in an arc to rifted arc setting upon crustal basement rocks of the Sandy Brook Group and Crippleback Intrusive Suite (Rogers et al. 2006; McNicoll et al. 2010; Zagorevski et al. 2010; Piercey et al. 2014). The Crippleback Intrusive Suite comprises the Crippleback Lake Pluton, which includes a quartz-monzonite that yielded a 563 Ma U-Pb zircon age, as well as the Valentine Lake and Lemottes Lake plutons (Rogers et al. 2006). The penecontemporaneous Sandy Brook Group consists of mafic and felsic volcanic rocks with continental arc characteristics (Rogers et al. 2006). The Bindons Pond Formation is dominated by felsic volcanic rocks (dacite to rhyolite), whereas the Lake Ambrose Formation is dominated by basalt, basaltic andesite, and andesite (Dunning et al. 1991; Evans and Kean 2002; Rogers et al. 2006; McNicoll et al. 2010; Piercey et al. 2014). Volcanogenic massive sulphide mineralization at the Duck Pond, Boundary, and Lemarchant deposits, as well as in several other areas within this formation and associated hydrothermal alteration are hosted by the Bindons Pond Formation (Squires et al. 1991; Squires and Moore 2004; McNicoll et al. 2010; Zagorevski et al. 2010; Piercey et al. 2014).

The Lemarchant deposit is hosted in the felsic volcanic rocks of the Bindons Pond Formation near the hanging wall mafic volcanic rocks of the Lake Ambrose Formation (Figs. 1b, 2). The contact between the formations is complex and often marked by intricate interdigitated of felsic and mafic volcanic rocks, with a thin (<1 to 20 m) layer of metalliferous mudstone. Most commonly, this exhalite layer occurs between the felsic and mafic volcanic rocks, either capping the massive sulphides, or at the same stratigraphic position distal from mineralization (Figs. 3a-c, 4a-c, respectively). Equally common are interflow mudstones occurring within the hanging wall basalts (Fig. 5a-c). The distribution of these metalliferous sedimentary rocks is discontinuous over one to four kilometres from the deposit (Copeland et al. 2009; Fraser et al. 2012).

Alteration at the Lemarchant deposit includes intense quartz, sericite and chlorite alteration, Ba-enrichment, anomalous disseminated and stringer-type pyrite, and base-metal sulphides with lesser amounts of pyrrhotite (Fraser et al. 2012). The majority of mineralization occurs as semi-massive to massive sulphide within the Lemarchant Main Zone, the Northwest Zone, and the smaller 24 Zone (Fig. 2; Copeland et al. 2009; Fraser et al. 2012). The indicated resources for the Lemarchant Main Zone currently are 1.24 Mt at 5.38% Zn, 0.58% Cu, 1.19% Pb, 1.01 g/t Au and 59.17 g/t Ag, with inferred resources of 1.34 Mt at 3.70% Zn, 0.41% Cu, 0.86% Pb, 1.00 g/t Au and 50.41 g/t Ag (Fig. 2; Fraser et al. 2012).

The Lemarchant Main Zone (Fig. 2) is 1.7 to 30.4 m thick and consists of a barite-rich outer zone that grades into a Pb-Zn-sulphide-rich zone, and an interior zone with Zn-Cu-sulphides that grades into stringer mineralization at depth (Copeland et al. 2009; Fraser et al. 2012; Gill and Piercey 2014; Gill 2015). In addition to typical VMS

sulphides (pyrite, sphalerite, galena, and chalcopyrite), the massive sulphides also contain tetrahedrite-tennantite, bornite, stromeyerite, and electrum (Copeland et al. 2009; Gill 2015). The trace elements and minor and major element mineral compositions of sulphides, sulphosalts, bornite, electrum, as well as barite, were studied in detail using LA-ICPMS (laser ablation-inductively coupled plasma mass spectometry) and EMPA (electron microprobe analysis) resulting in the detection of enrichments in Au, Ag, As, Hg ± Sb, Bi, Te in measured mineral phases occurring in the massive sulphides (Mercier-Langevin et al. 2011; Gill and Piercey 2014; Gill 2015). These elements are commonly recognized in precious metal-enriched VMS (Hannington et al. 1999; Mercier-Langevin et al. 2011). Additionally, bladed barite, calcite/Ca-Fe-Mg-Mn-carbonate and potassium feldspar alteration are common features in the deposit (Gill and Piercey 2014; Gill 2015). A combination of these petrological and lithogeochemical characteristics have led to the interpretation by Gill (2015) and Lode et al. (2015) that the Lemarchant deposit was a shallow water VMS deposit, with both VMS and epithermal features. The Lemarchant exhalites also contain many of the above main sulphide and other mineral phases, including bladed barite and calcite/Ca-Fe-Mg-Mn-carbonate, electrum ±Hg ±Sb, as well as acanthite and the Ag-Sb sulphosalts pyrargyrite and stephanite and also commonly display potassium feldspar alteration (Lode et al. 2015).

**Exhalite stratigraphy and lithofacies**

The Lemarchant exhalites occur either immediately on top of massive sulphide mineralization between the felsic and mafic volcanic rocks (exhalative mudstone-massive sulphide (EMS)-type; Fig. 3); extending laterally outwards from mineralization, but at the same stratigraphic level and without immediate association with mineralization (felsic-

exhalite-mafic (FEM)-type; Fig. 4); or as interflow mudstones within the hanging wall basaltic rocks (interflow exhalite (IFE)-type; Fig. 5). Interflow mudstones occur more frequently within 15 metres above the massive sulphide mineralization, but are present up to 70 meters above the ore horizon. Exhalites within the felsic volcanic rocks (FEF) below the ore horizon are only present in one drill hole (LM13-87), where it is found interdigitated with felsic volcanic rocks. These four exhalite types most commonly occur proximal and up to 200 m away from the mineralization of the Lemarchant Main Zone, but are also associated with the Northwest Zone, and in the area of the North target (Fig. 2).

The exhalites, independent of their stratigraphic positions, are brown to black, graphitic, finely laminated, and contain fine carbonaceous/organic-rich laminae that are intercalated with siliciclastic, volcaniclastic and/or amorphous kidney-shaped chert±apatite layers (Figs. 3a, 4a, 5a). The main sulphide phases are pyrite (framboidal, massive and euhedral; Fig. 6e-f) and pyrrhotite, with minor marcasite (Fig. 6f), chalcopyrite, sphalerite, arsenopyrite and galena (Fig. 6f-h). Contents of chalcopyrite, sphalerite, and galena increase proximal to mineralization (Fig. 7a-b). The sulphides occur both parallel to bedding, and in later stage, stringer-like veins (Figs. 3a, 4a, 5a, 7c-d). Locally, veins that cross-cut the original laminations, indicate diagenetic/tectonic remobilization and/or formation by intra-stratal synaeresis shrinkage cracks, which formed as de-watering structures (Füchtbauer et al. 1988; Harazim et al. 2013). Furthermore, stringer-type later stage veins have precious metal minerals including electrum ± Hg ± Sb (Fig. 7d-e) as well as acanthite, pyrargyrite and stephanite, which Lode et al. (2015) interpreted to be indicative of epithermal-style mineralization that is

overprinting the VMS-style mineral assemblage. Electrum, acanthite (Fig. 7d-f), pyrargyrite, stephanite, gersdorffite, cubanite, and digenite are rare, occurring as inclusions in pyrite, or interstitial to other sulphide phases. Electrum also occurs associated with pyrrhotite, arsenopyrite, chalcopyrite and galena (Fig.7e). All four types of exhalites have a high abundance of Ba minerals, including barite, celsian, hyalophane (Fig. 7g-h), and witherite.

**Exhalite sulphide and sulphate mineralogy**

Pyrite occurs as euhedral grains, as framboids, or as massive aggregates. The framboids are present as scattered single larger spheres (20-100 μm), as flocks of framboids, or as semi-massive framboid layers, consisting of small framboidal pyrite grains (1-10 μm; Fig. 6e). Dense layers of very fine-grained pyrite framboids commonly occur within the finely laminated mudstones. Pyrite tubes oriented parallel to lamination are also present in finely laminated carbonaceous exhalites. These pyritic tubes are partially overgrown by euhedral pyrite and arsenopyrite, and interstices between tubes are locally filled with chalcopyrite and sphalerite (Fig. 6g). Marcasite occurs as tabular crystals or blades in euhedral or massive pyrite (Fig. 6f), or as semi-continuous layers of marcasite clusters. Chalcopyrite occurs predominantly as interstitial grains between euhedral or framboidal pyrite and as a paragenetically late-stage phase in sulphide-rich layers parallel to the sedimentary lamination, or in cross-cutting veins (Figs. 6b, f-h, 7a-e). It is commonly associated with pyrrhotite, galena, sphalerite, and/or electrum. Chalcopyrite also forms pseudomorphs after euhedral pyrite and occurs as chalcopyrite-disease in sphalerite. Immediately proximal (<10 cm) to massive sulphides the sphalerite content increases significantly (Fig. 7a-b). Sphalerite on the contact between the massive

sulphides and the exhalites (5-70 cm wide zone) is Fe-rich (up to ~8 wt% Fe) red to purple sphalerite that grades down-stratigraphy into Fe-poor (<1 wt% Fe) white to honey brown sphalerite-dominated massive sulphides (Fig. 3a). Galena occurs as inclusions in, or interstitial to, euhedral pyrite, and is associated with chalcopyrite, sphalerite, electrum and, locally, pyrrhotite (Figs. 6h, 7b, d-e). Unlike in the more distal FEM- and IFE-type exhalites, in the proximal EMS-type exhalites galena is a major phase and is associated with sphalerite and euhedral or massive pyrite (Fig. 7b). Pyrrhotite occurs as disseminated patches in sulphide-poor mudstones or tuff, or as (semi-)continuous layers parallel to or cross-cutting mudstone laminations. Pyrrhotite is commonly associated with euhedral arsenopyrite and chalcopyrite, and locally with electrum (Fig. 7e). Ba-mineral phases include barite ($BaSO_4$), the Ba-rich feldspar celsian ($BaAl_2Si_2O_8$), and a barian K-feldspar with <2wt% Ba (hyalophane or barian adularia $(K,Ba)Al(Si,Al)_3O_8$). Barite forms anhedral (semi-)continuous layers or occurs as bladed crystals in vugs or veins, which are often associated with bladed Ca-Fe-Mg-Mn-carbonates. Barite-filled veins generally occur as crack-and-seal type veins, cross-cutting the exhalites and Pb-Zn-Cu sulphides (Fig. 7g-h). The Ba-feldspars are commonly present as paragenetically late minerals, with euhedral crystals overgrowing earlier phases such as pyrite framboids or barite (Fig. 7g-h). The Ba-carbonate witherite also occurs in the exhalites, but is less common than the other Ba-phases.

**Sulphur and Pb isotopes**

Representative exhalites were sampled for thin-section preparation and whole-rock analyses. Petrography of 184 thin-sections, which predominantly represented

various exhalite types, but also crystal lithic vitric tuff that is intercalated with the exhalites, and surrounding mafic and felsic volcanic lithologies. High resolution backscattered electron (BSE) images were obtained using a FEI Quanta 400 scanning electron microscope (SEM) at Memorial University, which is equipped with a Bruker energy dispersive x-ray (EDX) analytical system. Exhalites further selected for S and Pb isotopic studies included those that: 1) occur proximal to massive sulphides; i.e., are immediately associated with, or occur within five meters of mineralization (EMS-type) and represent the main stratigraphic marker between the felsic and mafic volcanic rocks (Bindons Pond and Lake Ambrose Formations, respectively); 2) do not have an obvious relationship with mineralization, but occur along the same stratigraphic contact between the felsic volcanic rocks of the Bindons Pond and mafic volcanic rocks of the Lake Ambrose formations (FEM-type); and 3) occur as interflow exhalites within the hanging wall Lake Ambrose Formation basalts (IFE-type).

Representative samples of these three types of exhalites (EMS, FEM, and IFE) were selected for secondary ion mass spectrometer (SIMS) microanalysis based on stratigraphic, spatial, textural and paragenetic relationships as deduced from field relationships. Pyrite (euhedral, massive, framboidal, spherical, and tube-like pyrite textures), pyrrhotite, chalcopyrite, arsenopyrite, and galena were analysed *in situ* for S isotopes using SIMS. Sulphide grains chosen for analysis were selected based on associated mineral assemblages, grain size, shape, and paragenesis. Overall, 210 $\delta^{34}S$ spot analyses of sulphides in 26 samples were measured, covering sections 100+50N to 108+00N (Fig. 2). To correct for instrumental mass fractionation (IMF) the following sulphide in-house standards were used: 1) pyrite – UL9 ($\delta^{34}S$ = +15.8‰) and KH87 ($\delta^{34}S$

= +0.2‰); 2) chalcopyrite – Norilsk ($\delta^{34}S$ = +8.3‰); 3) pyrrhotite – PoW1 ($\delta^{34}S$ = +2.3‰); 4) arsenopyrite – Arspy57 ($\delta^{34}S$ = +2.8‰); and 5) galena – HT10 ($\delta^{34}S$ = +14.2‰). Internal precision of individual $\delta^{34}S$ measurements was generally better than ±0.25‰ (1σ), with ±0.35‰ for the overall reproducibility.

Lead isotopes were analysed *in situ* by SIMS on inclusion free galena larger than >25 µm. Six samples yielded 38 spot analyses; spots for Pb isotope analyses were selected preferentially from the subset of samples that were previously analysed for S-isotopes. Seven data points were rejected based on poor data quality and the quality of the post-analysis SIMS pit left in the sample. Two in-house galena standards (F19 and JMBH) were used to correct for instrumental mass fractionation (IMF). 15 cycle analyses accumulated in 9 min routinely yield internal precisions (standard error of the mean) on $^{204}Pb/^{206}Pb$, $^{207}Pb/^{206}Pb$ and $^{208}Pb/^{206}Pb$ determinations of better than ±0.05 to 0.10% (1σ), while producing sputter craters only a few µm deep. Overall reproducibility, based on replicate analyses of the secondary standard JMBH, is typically better than ±0.10 – 0.15% for these same ratios. Samples were prepared and analysed following the methods described in detail in Brueckner et al. (2015) and Gill (2015) and described in Electronic Supplementary Material (ESM1).

## Results

### *Sulphur isotopes*

Pyrite has the widest range in $\delta^{34}S$ values; from -38.9‰ to +14.4‰ (ESM2). In detail, $\delta^{34}S$ analyses of euhedral pyrite (Figs. 6g-h,7a-e) have values between -26.1‰ and +14.4‰ (n = 70), with three populations: a) values ranging from -20‰ to -10‰; b) from

-2‰ to +6‰; and c) from +10.0‰ to +14.4‰ (Fig. 8). Pyrite framboids (Figs. 7c, 9a) have negative $\delta^{34}S$ signatures, with values ranging from -38.9‰ to -11.0 ‰ (n = 24), except one analysis with $\delta^{34}S$ of +12.2‰. Mats consisting of fine framboidal pyrite have $\delta^{34}S$ values that range from -16.9‰ to -5.7‰ (n = 6). Tube-like pyrite from two laminae in brown, finely laminated sulphide-rich exhalite, (Fig. 6c, g) have $\delta^{34}S$ values between -30.5‰ and -20.1‰ (n = 2). The three marcasite samples, including framboidal and euhedral marcasite (Fig. 6f), have a very restricted $\delta^{34}S$ of between -13.1‰ to -12.4‰. Arsenopyrite (Figs. 6g, 7e) and pyrrhotite (Fig. 7e) have similar $\delta^{34}S$, ranging from -24.4‰ to -10.5‰ (n = 11) and -23.7‰ to -8.1‰ (n = 24), respectively. Chalcopyrite has $\delta^{34}S$ that ranges from -22.8‰ to +3.2‰ (n = 43; Figs. 6-h, 7a-c, e), and galena has values from -20.0‰ to +12.0‰ (n = 26) (Figs. 6e, 7b, d). Both chalcopyrite and galena show two populations: at -20‰ to -10‰ and -2‰ to +6‰ (Fig. 8). Notably, euhedral pyrite, chalcopyrite, and galena in exhalites proximal to Main Zone mineralization tend towards positive $\delta^{34}S$ signatures (Fig. 10b; ESM2). In contrast, pyrite framboids, arsenopyrite, and pyrrhotite do not show distinct spatial variations in $\delta^{34}S$ (Fig. 9a-c). Exhalites closely related to massive sulphides (EMS-type) have more positive $\delta^{34}S$ values than interflow exhalites (IFE-type); FEM-type exhalites have intermediate values between the EMS- and IFE-type exhalites (Fig. 10a-b).

*Lead isotopes*

Galena lead isotope data are summarized in ESM3. Overall, the data form clusters, yielding overall ranges of $^{206}Pb/^{204}Pb$ = 18.03-18.23, $^{207}Pb/^{204}Pb$ = 15.40-15.81, and $^{208}Pb/^{204}Pb$ = 37.35-39.01, respectively. Nevertheless, in EMS-type exhalites small variations in $^{206}Pb/^{204}Pb$ are discernable, and the $^{207}Pb/^{204}Pb$ and $^{208}Pb/^{204}Pb$ ratios are

more highly variable. EMS-type mudstones have less radiogenic $^{206}Pb/^{204}Pb$ ratios than those exhalites that have no immediate association with massive sulphides (FEM); and both groups lie on subparallel trends with distinctive $^{206}Pb/^{204}Pb$ (Fig. 11a-b).

EMS-type exhalites yield average $^{206}Pb/^{204}Pb$, $^{207}Pb/^{204}Pb$, and $^{208}Pb/^{204}Pb$ ratios of 18.09 ±0.12, 15.53 ±0.15, and 37.67 ±0.16, respectively, and range from 18.03-18.19, 15.40-15.62, and 37.35-38.05, respectively. These values overlap, for the most part, with the results for bulk galena samples in the Lemarchant massive sulphides (Fig. 11a-b; Gill 2015; Pollock and Wilton 2001).

FEM-type exhalites have slightly more radiogenic $^{206}Pb/^{204}Pb$ ratios relative to the EMS-type, with an average of 18.16 ±0.14, but similar $^{207}Pb/^{204}Pb$ and $^{208}Pb/^{204}Pb$ ratios with averages of 15.54 ±0.18 and 37.76 ±0.20, respectively. The FEM-type exhalites have $^{206}Pb/^{204}Pb$, $^{207}Pb/^{204}Pb$, and $^{208}Pb/^{204}Pb$ that range from 18.03-18.23, 15.45-16.61, and 37.65-37.93, respectively. These FEM-type samples plot along a trend towards the more radiogenic Duck Pond hydrothermal metalliferous mudstones (Fig. 11a-b; Piercey *unpublished data*). One FEM-galena outlier plots at the least radiogenic end of the $^{207}Pb/^{204}Pb$ and $^{208}Pb/^{204}Pb$ cluster, but the analytical errors are larger than those of the other samples and therefore, the significance of this analysis is uncertain. Overall, the EMS- and FEM-type mudstones have similar $^{207}Pb/^{204}Pb$ and $^{208}Pb/^{204}Pb$ and the $^{206}Pb/^{204}Pb$ values overlap within analytical error; however 2σ error ellipses calculated with Isoplot 3.75 suggest that the $^{206}Pb/^{204}Pb$ of the EMS- and FEM-mudstones form two separate clusters (Fig. 11a-b). Additionally, a t-test was conducted to compare the means of the EMS- and FEM-mudstones Pb data ($M_{EMS}$ = 18.09, $STDEV_{EMS}$ = 0.037; $M_{FEM}$ = 18.18, $STDEV_{FEM}$ = 0.023) and a significant difference was detected with t = 6.59 and p

(two-tailed) < 0.001 at a confidence level of 95%. These results confirm that the Pb-data of EMS- and FEM-mudstones represent two statistically distinct populations.

From the 31 analysed Pb isotope spots measured on galena, 25 (from 6 samples) were also measured for sulphur isotopic compositions (15 EMS-type; 10 in the FEM-type). Notably, the majority of galena samples in EMS-type exhalites have predominantly positive $\delta^{34}S$ isotopic signatures (-1.2‰ to +5.9‰) and are associated with lower (less radiogenic) $^{206}Pb/^{204}Pb$ isotopic compositions (Fig. 12a-c). In contrast, FEM-type exhalites have negative $\delta^{34}S$ values (-18.0 ‰ to -14.5‰) and have more radiogenic $^{206}Pb/^{204}Pb$ isotopic ratios (Fig. 12a-c). The $^{207}Pb/^{204}Pb$ and $^{207}Pb/^{204}Pb$ ratios show less distinction between EMS- and FEM-type mudstones. Two galena Pb isotope analyses of the EMS-type exhalites have negative $\delta^{34}S$ (-14.7‰) but Pb isotope ratios that fall within the ranges of the other EMS galena (Fig. 12a-c).

## Discussion

### Sulphur isotopic composition of exhalites and the role of bacteria/archaea

A hydrothermal origin and formation from black smoker plume fallout of the sulphide-bearing exhalites of the Lemarchant deposit was proposed by Lode et al. (2015). Hydrothermal exhalites, including those from Lemarchant, have similar sulphur sources to the associated massive sulphides, including sulphur derived from both inorganic and organic processes (Ohmoto and Rye 1979; Ohmoto and Goldhaber 1997; Huston 1999; Seal 2006; Alt and Shanks 2011).

In VMS deposits the main sources of inorganic sulphur are thermochemical sulphate reduction (TSR) of seawater sulphate, and sulphur leached from igneous and/or sedimentary rocks. TSR-derived $H_2S$ forms during hydrothermal circulation via the

reaction of heated seawater sulphate (T>150ºC) with ferrous silicates and oxides within the wallrock (Ohmoto and Rye 1979; Shanks et al. 1981; Ohmoto and Goldhaber 1997; Shanks 2001; German and Von Damm 2003; Seal 2006; Tivey 2007; Huston et al. 2011).

Pyrite-rich polymetallic sulphides in Phanerozoic VMS deposits have $\delta^{34}S$ values in sulphides that are ~18‰ to 25‰ lower than the $\delta^{34}S$ of seawater at the time of formation (Sangster 1968; Ohmoto and Goldhaber 1997; Huston 1999; Seal 2006). In contrast, igneous sources are much more restricted, and high temperature (~350°C) leaching of sulphides from basement rocks generally yields massive sulphides with $\delta^{34}S$ values of 0±3‰, (Ohmoto and Rye 1979; Shanks et al. 1987; Campbell and Larson 1998; Shanks 2001). Degassing of magmatic sulphur yields sulphides with $\delta^{34}S$ ~0‰. However, significant $\delta^{34}S$ variations can occur due to magmatic disproportionation of $SO_2$ in magmatic volatiles, yielding sulphides with substantially more variable $\delta^{34}S$ (Woodruff and Shanks 1988; Shanks 2001; Seal 2006).

To predict the expected range of $\delta^{34}S$ for TSR-derived sulphur isotopes in pyrite, pyrrhotite, chalcopyrite, and galena in the Lemarchant exhalites, modelling was undertaken following modified methods described in Brueckner et al. (2015) and Cloutier et al. (2015). Due to a lack of reliable experimental fractionation data for arsenopyrite, no modelling was undertaken on arsenopyrite. For the modelling of pyrite, pyrrhotite, chalcopyrite, and galena, an estimated $\delta^{34}S$ of +34.5‰ was used for Cambrian seawater (Kampschulte and Strauss 2004; Seal 2006), and TSR was modelled over the range of 250°C to 350°C, a typical temperature range for VMS-related settings (Shanks et al. 1981). Based on this modelling, expected $\delta^{34}S$ values for pyrite range from +11.1 to +16.6‰, for pyrrhotite from +10.0 to +15.4‰, for chalcopyrite from +9.4 to +15.0‰,

and for galena from +7.3 to +13.5‰ (Fig. 13a-d), implying that some Lemarchant exhalites have a component of TSR-derived sulphur. However, TSR cannot explain the entire range $\delta^{34}S$ observed. For example, the measured $\delta^{34}S$ values of pyrite ranging from -22.4‰ to +14.4‰ can be explained by mixing of TSR- and biogenically-derived sulphur, with >0 to 100% contributions of TSR-derived sulphur, respectively (Fig. 14a). However, according to the modelling, values of below -22.4‰ have no TSR-contributions at all, which indicates to biogenically-derived sulphur only (Fig. 14a).

Accordingly, the Lemarchant exhalites show evidence for significant biogenically-derived sulphur. In general, the main source of organic $H_2S$ is expected to be from microbial/biogenic (bacteria and archaea) reduction of seawater sulphate (BSR) at temperatures <120°C (Thode et al. 1951; Kaplan and Rittenberg 1964; Shanks et al. 1981; Canfield 2001a; Canfield 2001b; Shanks 2001; Seal 2006; Konhauser 2007; Alt and Shanks 2011). The currently known and measured upper limit of temperature for the growth of organisms is achieved by Archea with 121°C, and by hyperthermophile sulphate-reducing bacteria with 110°C that live in hot sediments around deep-sea hydrothermal vents (Gottschal and Prins 1991; Jørgensen et al. 1992; Elsgaard et al. 1994; Konhauser 2007).

Maximum fractionation of ~40 to 45‰ from the $SO_4^{2-}$ reservoir being reduced were obtained from natural microbial populations and laboratory cultures (Kemp and Thode 1968; Habicht and Canfield 1997; Canfield 2001a; Habicht and Canfield 2001). This process commonly occurs in semi-permeable sediments, near the interface to the oxygenated ambient seawater, and can take place as long as there is an $SO_4^{2-}$ supply,

sufficient organic matter, and temperatures remain <120°C (Habicht and Canfield 1997; Habicht and Canfield 2001; Seal 2006).

Pyrite-framboids are a common by-product of BSR-related processes. However, biogenically-produced $H_2S$ can be fixed into sulphides with any kind of metals (or metalloid) present in the pore-fluids, not only $Fe^{2+}$, but also including hydrothermally derived $Cu^{+}$, $Zn^{2+}$, $Pb^{2+}$, and As. Both pyrite framboids, and these base metal sulphides, are expected to yield negative $\delta^{34}S$ values, characteristic of biogenically-derived sulphur. On the other hand, positive $\delta^{34}S$ values only do not exclude the presence of microbial sulphate reduction. If hydrothermal fluids with TSR-derived $H_2S$ contribute to the pore-fluids in the hydrothermal exhalites, as shown above, the precipitated sediment-hosted sulphides will have mixed sulphur-signatures with $\delta^{34}S$ ranging from negative to positive values.

The Lemarchant exhalites display mixed sulphur isotope signatures consistent with both TSR- and biogenically-derived sulphur components (Fig. 10a). The negative $\delta^{34}S$ values in the exhalites imply significant microbial $H_2S$ in the sulphides. There is a variation within this BSR signature, with exhalites distal from mineralization having lower $\delta^{34}S$ than those proximal (EMS-type) suggesting a greater input from hydrothermal TSR (or direct or leached magmatic S) (Figs. 9a, c, and 10b). To quantify the relative roles of biogenically- and TSR-derived sulphur two component mixing modelling was undertaken. For these calculations the biogenic sulphur reservoir was assumed to have an average $\delta^{34}S$ of -25‰, which is reflected by the lower end of the bulk of the polymetallic sulphide data (Fig. 10a). The same estimate of $\delta^{34}S$ of +34.5‰ for Cambrian seawater (Kampschulte and Strauss 2004) was used, as well as a temperature of 300°C for

producing TSR-derived $H_2S$. The temperature of 300°C for the TSR-derived $H_2S$ reflects the assumption that the Lemarchant hydrothermal system likely did not reach much higher temperatures than 300°C, based on the lack of abundant chalcopyrite in the massive Pb-Zn-sulphides. For BSR-derived $H_2S$ temperatures of 0°C, 50°C, 100°C, and 120°C were chosen to calculate the mixing lines, bracketing the known temperature ranges at which bacteria/archaea can thrive (Jørgensen et al. 1992; Elsgaard et al. 1994; Ohmoto and Goldhaber 1997). Results from mixing calculations illustrate that pyrrhotite samples contain 0% to 48% TSR-derived sulphur (Fig. 14b). The close spatial association of arsenopyrite with pyrrhotite, and its low $\delta^{34}S$ (Figs. 9a, 10b), suggest both minerals have a biogenic-diagenetic origin, i.e., are predominantly co-genetically formed, when reactions with organic matter causes low $fO_2$ and conditions favouring arsenopyrite and pyrrhotite precipitation (Hannington et al. 1995). In contrast, chalcopyrite and galena have between ~5% and 82%, and ~20% to 100% of TSR-derived sulphur, respectively, indicating a greater hydrothermal sulphur input into their genesis (Fig. 14c-d). The variability of pyrite $\delta^{34}S$ also indicates TSR-BSR mixing, with euhedral pyrite having a greater TSR sulphur component. Conversely, the pyrite-framboids have BSR-derived sulphur only (Fig. 9a).

For EMS-type exhalites, however (Fig. 7a-b), those proximal to massive sulphide mineralization have values that are lower than those typically expected simply from TSR of Cambrian seawater (Kampschulte and Strauss 2004). As these depleted values could be attributed to BSR, textural evidence suggests that there is potential that they have contributions from igneous sources. This seems possible, because the igneous-like signatures are found in euhedral pyrite, chalcopyrite, and galena, proximal to massive

sulphide mineralization (Fig. 7a-b), which are also associated with electrum ± Hg ± Sb (Fig. 7d-e) as well as acanthite (Fig. 7f), pyrargyrite, stephanite (Lode et al. 2015). These near zero $\delta^{34}S$ values are similar to values expected from igneous sources; however, the nature of the igneous source (i.e., leaching from basement vs. magmatic fluids) is difficult to determine unequivocally with sulphur isotopes alone. Nevertheless, the more negative $\delta^{34}S$ values are potentially more closely affiliated with magmatic fluids, as magmatic disproportionation and subsequent $SO_2$ condensation is known to produce $H_2S$ and sulphides with $\delta^{34}S<0$ (Rye 1993; Huston et al. 2011). This suggested sulphur source would also be consistent with the mineral associations, elevated contents of Au, Ag, As, Hg ± Sb, Bi, Te, and the sulphosalt-rich mineralogy of the underlying massive sulphides in the Lemarchant deposit (Gill and Piercey 2014; Gill 2015; Lode et al. 2015). Precious metal enrichment and post-VMS mineralization potassium feldspar alteration further support the previous interpretations that suggest a possible magmatic input into the Lemarchant VMS system in a shallow water tectonic setting that allows boiling (Hannington et al. 1999; Mercier-Langevin et al. 2011; Gill and Piercey 2014; Gill 2015; Lode et al. 2015). This type of precious metal bearing VMS-epithermal deposits are known to occur in shallow water environments associated with arc rifting (Sillitoe et al. 1996; Hannington et al. 1999; Mercier-Langevin 2011); a tectonic environment which is suggested for the Lemarchant deposit and the Tally Pond belt (Piercey et al. 2014; Lode et al. 2015).

In addition to near zero $\delta^{34}S$ values, there are also some extremely negative values in pyrite (i.e., $\delta^{34}S < -25‰$), which are much lower than can be reasonably explained by BSR only, taking fractionation factors of ~45‰ into account (Habicht and Canfield 1997;

Canfield 2001a; Habicht and Canfield 2001). Even if seawater sulphate showed substantial variation in the Cambrian (e.g., $\delta^{34}S$ = +28.8‰ to 34.5‰; Sangster 1968; Kampschulte and Strauss 2004), this would only yield values $\delta^{34}S$ values from BSR from -16.2‰ to -10.5 (Habicht and Canfield 1997; Canfield 2001a; Habicht and Canfield 2001). Accordingly, another process for $^{34}S$ depletion in the sulphur isotopic system is required to create the large fractionation (up to 73‰; Fig. 10a) in these samples. We propose that these low values are due to sulphide-oxidizing bacteria and microbial disproportionation of sulphur intermediates. Large fractionation, up to 72‰, for single-step microbial sulphate reduction is reported by Wortmann et al. (2001) from deep (>20 m below seawater surface) pore-waters in a carbonate ramp. This process may represent another possibility to cause large fractionation (Wortmann et al. 2001). However, the deep brine poor water environment in carbonate rocks is a rare setting and their microbial communities likely are different from those occurring in microbial mats at the sediment-water interface in a hydrothermal environment (Wortmann et al. 2001).

Sulphide oxidizing bacteria (e.g., microbial mats of *Beggiatoa* sp.) are known to occur in ridge environments, and often found as surface films on sulphidic sediments associated with sulphate reducers, and to create some of the largest fractionation reported (Kaplan and Rittenberg 1964; Jørgensen 1990; Elsgaard et al. 1994, Frank et al. 2013). These *Beggiatoa* sp. mats are found around hydrothermally active sites, such as in the Guaymas Basin (Elsgaard et al. 1994). The biogenic oxidation (BSO) involves non-phototrophic oxidation of reduced sulphur compounds ($H_2S$, $S_0$) and is coupled to the microbial disproportionation of sulphur intermediate compounds (Canfield 2001b). These biologically-mediated processes fractionate sulphur isotopes towards more negative

values, and more importantly, the products of microbial fermentation and thermal degradation of organic matter provide the substrate that is required for microbial/biogenic $SO_4^{2-}$ reduction (BSR) (Kaplan and Rittenberg 1964; Jørgensen 1990; Elsgard et al. 1994, Canfield 2001b). Thereby, fermentative microbes decompose dead microbial biomass, which stimulates BSR (Elsgard et al. 1994). These diverse microbial communities (chemolithotrophic bacteria/archaea) are also commonly found around hydrothermal vent sites and in areas of diffuse venting, as in exhalites (Gottschal and Prins 1991; Elsgaard et al. 1994; Hannington et al. 1995; Canfield 2001a; Canfield 2001b; Frank et al. 2013), which would be consistent with their presence in the Lemarchant exhalites. Furthermore, the very common finely laminated texture (Fig. 6a-d), stromatolite-like bulbous layers in finely laminated mudstone and chert (Konhauser 2007; Fig. Ia-b, ESM4), and bands in the mudstones containing tubes of pyrite with interstitial chalcopyrite and sphalerite with a general textural robustness, are all features consistent with an origin from microbial mats (Berkenbosch et al. 2012; Schieber, J. *pers. comm.*; Fig. 6c, g).

Microbial mats can serve as the nucleus for mineral growth, and microbially mediated changes in pH and $fO_2$ can induce local sulphide precipitation, which can influence the isotopic compositions of the mineralizing sulphides and sulphates (Jørgensen et al. 1992). Chemolithoautotrophic microbial mat-forming bacterial and archaeal communities consist not only of sulphate-reducers and -oxidizers, but also of microbial species that gain the energy necessary for their metabolism via microbial disproportionation of sulphur intermediate compounds, such as elemental sulphur ($S^0$), thiosulphate ($S_2O_3^{2-}$), and sulphite ($SO_3^{2-}$) (Figs. 15, 16b; Bak and Pfennig 1987; Jørgensen 1990; Jørgensen et al. 1992; Canfield 2001b; Konhauser 2007). The $SO_4^{2-}$

produced via microbial disproportionation can thus then be further utilized for BSR, resulting in a cyclic process involving various species of sulphur. Microbial disproportionation of sulphur intermediate compounds is a process that can cause further $^{34}S$ depletion in the produced sulphide of up to ~6‰ and can be described with following reactions (Bak and Pfennig 1987; Jørgensen 1990; Habicht and Canfield 1997; Canfield 2001a):

$$S_2O_3^{2-} + H_2O \Rightarrow H_2S + SO_4^{2-} \quad (1)$$

$$4SO_3^{2-} + 2H^+ \Rightarrow H_2S + 3SO_4^{2-} \quad (2)$$

$$4S^0 + 4H_2O \Rightarrow 3H_2S + SO_4^{2-} + 2H^+ \quad (3)$$

Reaction (1) does not require an electron donor or acceptor, and is biologically catalysed. However, in the presence of Fe-oxyhydroxides and organic matter, which are both common in hydrothermal sediments, microbes can utilize these phases as electron acceptor and donor, respectively (Jørgensen 1990):

$$S_2O_3^{2-} + CH_3COO^- + H^+ \Rightarrow 2HS^- + 2CO_2 + H_2O \quad (4)$$

$$S_2O_3^{2-} + 8FeOOH + 14H^+ \Rightarrow 2SO_4^{2-} + 8Fe^{2+} + 11H_2O \quad (5)$$

The FEM-type exhalite sample shown in Figure 6c and g contains two ~1 mm thick bands of sulphide in a finely laminated carbonaceous exhalite. These bands consist of pyrite tubes with interstitial chalcopyrite and sphalerite, as well as arsenopyrite. The sulphur isotopic analysis of one these tubes yielded a $\delta^{34}S$ of -30.5‰, which implies additional biogenic sulphur sources other than BSR, such as BSO and microbial disproportionation. Therefore, it is suggested that the tubes are microbial in origin, and that the two ~1 mm thick bands reflect sulphidized mats of microbial filaments. The interstitial chalcopyrite, sphalerite, and arsenopyrite - which display mixed, biogenically-

and TSR-derived sulphur sources - were precipitated from later-stage metalliferous fluids overprinting earlier formed tubes. Similar microbial tubes are reported related to modern black smoker chimneys of the Brothers submarine volcanoes in the Kermadec Arc (Berkenbosch et al. 2012).

Figure 15 delineates the process pathway for sulphur isotopic compositions occurring in sedimentary sulphides. In this scheme, initial sulphate reduction (BSR and/or TSR) is followed by an intermediate step of sulphide oxidation. Subsequent microbial disproportionation of sulphur intermediate compounds creates $H_2S$ that is further depleted in $^{34}S$, and $SO_4^{2-}$ that can be further utilized in the reduction processes (Canfield 2001a). A combination of cycling and cumulative $^{34}S$ depletion during these microbial processes (BSR, BSO, microbial disproportionation), provides a plausible explanation of the large fractionation (>45‰) observed in hydrothermal sedimentary sulphides in the Lemarchant exhalite pyrite.

*Open versus closed system conditions*

Microbial sulphate reduction, and the isotopic composition of precipitated BSR-related sulphides, depend on whether there is a limited (closed) or unlimited (open) source of seawater $SO_4^{2-}$ (Kemp and Thode 1968; Ohmoto and Goldhaber 1997). In many ore deposits, whether the system is open or closed depends on whether more $SO_4^{2-}$ is available for reduction than $SO_4^{2-}$ is reduced, which in turn can have influence on the nature, preservation and processes of sulphide deposition (Goodfellow and Peter 1996). Seal et al. (2000) and Seal (2006) produced model histograms of $\delta^{34}S$ distribution for sedimentary sulphides as a function of whether the environment was open or closed to

seawater sulphate. Narrow, restricted ranges in $\delta^{34}S$ represent open system conditions, whereas wide ranging $\delta^{34}S$ reflects near closed-system conditions. Transitional patterns represent partially closed and open system conditions (Seal 2000; Seal 2006). The distribution of $\delta^{34}S$ in the Lemarchant exhalites suggests deposition under open to partially closed conditions (Fig. 8). However, the presence of abundant barite at Lemarchant, and the rare-earth element patterns in the Lemarchant exhalites, are consistent with deposition from an oxygenated water column (Lode et al. 2015). Therefore, the variation in $\delta^{34}S$ values in the frequency histograms for Lemarchant hydrothermal mudstone sulphides (Fig. 8) are interpreted as due to mixing between hydrothermal, inorganically TSR-derived sulphur and biogenic sulphur on the flanks of the sulphide mound. Oxygenated open system conditions are further supported by the presence of marcasite in the Lemarchant exhalites. In most cases, marcasite partially replaces pyrite and it is suggested that marcasite formed paragenetically late, after the higher temperature hydrothermal system ceased, because marcasite has higher growth rates and dominates over pyrite at lower temperatures and acidic conditions (pH <5) (Murowchick and Barnes 1986; Schoonen and Barnes 1991; Schieber 2011). Pyrite associated with the euhedral marcasite shows locally corrosion textures that are likely due to partial re-oxidation (Schieber 2011). This partial oxidation of pyrite is caused by the oxygenated ambient waters and creates conditions that favour marcasite precipitation (Schieber 2011).

Lead isotopic composition of hydrothermal mudstones

The Pb sources in VMS are derived predominantly from leached basement rocks, which can have varying Pb isotope signatures and may contain Pb from different reservoirs, depending on their origin (Franklin et al. 1981; Swinden and Thorpe 1984; Tosdal et al. 1999; Ayuso et al. 2003). Lead isotopes in the Lemarchant exhalites were measured *in situ* on galena, which is used as a proxy for the Pb in other sulphide phases. This is supported by both paragenetic relationships, e.g., that galena is paragenetically and spatially associated with chalcopyrite (Fig. 7b, d, e), suggesting deposition from the same hydrothermal fluid.

The galena Pb isotopic composition of the Lemarchant exhalite overlaps with values from various massive sulphide deposits in the Tally Pond Belt, including the Lemarchant massive sulphides (Fig. 11a-b; Swinden and Thorpe 1984; Pollock and Wilton 2001; Gill 2015; Piercey *unpublished data*). The observed variations in Pb isotope ratios require derivation from juvenile to more evolved crustal sources (Fig. 11a-b). Leaching of basement rocks could explain the Pb isotope variations, as the underlying stratigraphy of the Sandy Brook Group is bimodal, with mafic to felsic rocks that have varying isotopic signatures (Rogers et al., 2006). Further, the entire Victoria Lake Supergroup is of peri-Gondwanan affinity and has a peri-continental character (Rogers et al. 2006; Zagorevski et al. 2010). Thus, variations from more continental to juvenile sources are plausible (Swinden and Thorpe 1984; Rogers et al. 2006; Zagorevski et al. 2010). The overlapping clusters of the EMS-type exhalites and the massive sulphides of the Lemarchant deposit suggest that they have the same Pb source.

Whereas leaching of basement Pb can explain the absolute variation in exhalite Pb isotope compositions, the presence of more radiogenic Pb isotope signatures in distal

FEM-type exhalites relative to the more juvenile signature in EMS-type exhalites proximal from mineralization cannot be explained by leaching of basement sources alone. This suggests a more radiogenic detritally-derived Pb source, which is characterized by more radiogenic $^{206}Pb/^{204}Pb$ and $^{208}Pb/^{204}Pb$ ratios, contributing to the FEM-type exhalites (Mills and Elderfield 1995). The less radiogenic $^{206}Pb/^{204}Pb$ ratios of the proximal EMS-type mudstones and massive sulphides at Lemarchant indicate that those have only minimal detrital Pb contributions. Interestingly, the FEM-type exhalites with more radiogenic $^{206}Pb/^{204}Pb$ also yield $\delta^{34}S$ values that indicate to less TSR-derived hydrothermal sulphur, whereas proximal EMS exhalites have a lower, more juvenile $^{206}Pb/^{204}Pb$ and a strong TSR-derived hydrothermal $\delta^{34}S$ signature (Fig. 12a). This correspondence of low $\delta^{34}S$ and more juvenile Pb isotopic signatures may also serve as a vector towards mineralization in proximal environments in other metalliferous mudstones in the Lemarchant deposit area and in VMS deposits in similar arc settings.

## Conclusions

The Lemarchant hydrothermal exhalites record different S sources and processes. The exhalites precipitated prior to, during, and after the formation of massive sulphide mineralization. The majority of the sulphides hosted in the Lemarchant exhalites have mixed inorganic and organic sulphur sources and processes, including: 1) sulphur derived from thermochemical reduction of seawater sulphate; 2) biogenic sulphur; and 3) potential magmatic contributions by either leaching of crustal rocks and/or possibly a direct magmatic fluid/volatile input. The biogenic processes (bacterial/archaeal) involved in the sulphur isotope fractionation in the Lemarchant exhalites include: 1) the biogenic/microbial reduction of seawater sulphate; 2) the microbial disproportionation of

sulphur intermediates; and 3) an intermediate step of biogenic sulphide oxidation. These organic processes occurred within microbial mats that covered the sulphide-rich metalliferous sediment, which may have also helped to consolidate the exhalites, enhancing sulphide precipitation. Despite the presence of abundant negative $\delta^{34}S$ values and the importance of biogenic processes, exhalites closely associated with massive sulphides have greater TSR-derived S, and potentially igneous/magmatic S contributions, than interflow exhalites and exhalites that have no immediate association with mineralization.

Lead isotopes in galena from the Lemarchant exhalites suggest they have both juvenile and more radiogenic Pb sources. The mixed Pb source is consistent with derivation from underlying basement rocks. In exhalites proximal to mineralization, however, there is a correspondence between lower $^{206}Pb/^{204}Pb$ ratios and more positive $\delta^{34}S$ values within the range of TSR, suggesting that these exhalites had a greater hydrothermal component and juvenile Pb derived from leaching of mafic volcanic basement rocks. More distal exhalites however have higher $^{206}Pb/^{204}Pb$ ratios suggesting an additional detrital Pb source contributing to the more distal depositional environments. The correspondence of juvenile Pb and hydrothermal $\delta^{34}S$ derived from TSR may be a useful vector for proximity to mineralization in hydrothermal exhalites, and in other VMS hydrothermal systems in similar exhalative environments globally.

**Acknowledgements**

This research is funded by the Canadian Mining Research Organization (CAMIRO) and an NSERC CRD grant. Kind support was provided by Dianne and Charlie Fost, Michael Vande Guchte, Alexandria Marcotte, and Gerry Squires from

Paragon Minerals Corporation (now Canadian Zinc Corporation). Research is also funded by the NSERC-Altius Industrial Research Chair in Mineral Deposits, funded by NSERC, Altius Resources Inc., and the Development Corporation of Newfoundland and Labrador. The authors would like to thank for the help and support from Keir Hiscock, Pam King, Michael Buschette, Shannon Gill, Shannon Guffey, Dario Harazim, and Inês Nobre Silva. Also very much appreciated are the reviews and suggestions of the *Mineralium Deposita* reviewers, David Huston and Fernando Tornos, and the Editor-in-Chief Georges Beaudoin, which greatly improved the manuscript.

## References

Alt JC, Shanks WC (2011) Microbial sulphate reduction and the sulphur budget for a complete section of altered oceanic basalts, IODP Hole 1256D (eastern Pacific). Earth Planet Sci Lett 310:73-83. doi: 10.1016/j.epsl.2011.07.027.

Ayuso RA, Wooden JL, Foley NK, Slack JF, Sinha AK, Persing H (2003) Pb isotope geochemistry and U-Pb zircon (SHRIMP-RG) ages of the Bald Mountain and Mount Chase massive sulphide deposits, northern Maine; mantle and crustal contributions in the Ordovician. Econ Geol Monographs 11:589-609.

Bak F, Pfennig N (1987) Chemolithotrophic growth of Desulfovibrio sulfodismutans sp. nov. by disproportionation of inorganic sulfur compounds. Arch Microbiol 147:184-189.

Berkenbosch HA, de Ronde CEJ, Gemmell JB, McNeill AW, Goemann K (2012) Mineralogy and formation of black smoker chimneys from Brothers submarine volcano, Kermadec Arc. Econ Geol 107:1613-1633. doi: 10.2113/econgeo.107.8.1613.

Binns RA (2004) Eastern Manus Basin, Papua New Guinea: guides for volcanogenic massive sulphide exploration from a modern seafloor analogue In: McConachy TF, McInnes BIA (eds) CSIRO Explores. pp 59-80.

Boström K, Peterson MN (1966) Precipitates from hydrothermal exhalations on East Pacific Rise. Economic Geology 61:1258-&.

Boström K, Peterson MN, Joensuu O, Fisher DE (1969) Aluminum-poor ferromanganoan sediments on active oceanic ridges. Journal of Geophysical Research 74:3261-&. doi: Doi 10.1029/Jb074i012p03261.

Bottrell SH, Newton RJ (2006) Reconstruction of changes in global sulphur cycling from marine sulphate isotopes. Earth-Sciences Reviews 75:59-83.

Brueckner SM, Piercey SJ, Layne GD, Piercey G, Sylvester PJ (2015) Variations of sulphur isotope signatures in sulphides from the metamorphosed Ming Cu(-Au)

volcanogenic massive sulphide deposit, Newfoundland Appalachians, Canada. Miner Deposita 50:619-640.

Campbell AR, Larson PB (1998) Introduction to stable isotope applications in hydrothermal systems. In: Richards JP, Larson PB (eds) Techniques in Hydrothermal Ore Deposits Geology. Reviews in Econ Geol, pp 173-193.

Campbell IH, Lesher CM, Coad P, Franklin JM, Gorton MP, Thurston PC (1984) Rare-earth element mobility in alteration pipes below massive Cu-Zn sulphide deposits. Chemi Geol 45:181-202.

Canadian Zinc Corporation Press Release December 11, 2013 available at: www.canadianzinc.com/images/Docs/News_Releases/CZNNR20131211.pdf www.sedar.com/DisplayCompanyDocuments.do?lang=EN&issuerNo=00002753

Canfield DE (2001a) Isotope fractionation by natural populations of sulphate-reducing bacteria. Geochim Cosmochim AC 65:1117-1124.

Canfield DE (2001b) Biogeochemistry of sulphur isotopes. Rev Mineral Geochem 43:607-636. doi: 10.2138/gsrmg.43.1.607.

Cloutier J, Piercey SJ, Layne GD, Heslop JB, Hussey AM (2015) Styles, textural evolution and sulphur isotope systematics of Cu-rich sulphides from the Cambrian Whalesback volcanogenic massive sulphide (VMS) deposit, Central Newfoundland, Canada. Econ Geol.

Copeland DA (2009) Assessment report on prospecting, lithogeochemical sampling and data interpretation on the Harpoon Property (Licenses 7695M, 10461M, 10464M, 10465M, 10607M, 12357M, 12885M, 13583M, 13448M, 13449M and 13667M) and the South Tally Pond Property (Licences 8183M, 9569M and 14158M) Lake Ambrose Area, Newfoundland and Labrador. NTS 12A/10 and 12A/07. Paragon Minerals Corporation.

Copeland DA, Toole RM, Piercey SJ (2009) 10th year supplementary assessment report on soil sampling, linecutting, Titan 24 Geophysical Surveying, Diamond Drilling and Petrography, Licence 8183M, South Tally Pond Property, Rogerson Lake Area, Newfoundland and Labrador, NTS 12A/10 and 12A/07. Newfoundland and Labrador Geological Survey Assessment File, St. John's, NL, Canada, pp 56.

Canadian Zinc Corporation (2013) Press release, December 11.

Dias AS, Mills RA, Taylor RN, Ferreira P, Barriga FJAS (2008) Geochemistry of a sediment push-core from the Lucky Strike hydrothermal field, Mid-Atlantic Ridge. Chem Geol 247:339-351.

Dunning GR, Kean BF, Thurlow JG, Swinden HS (1987) Geochronology of the Buchans, Roberts Arm, and Victoria Lake groups and Mansfield Cove Complex, Newfoundland. Can J Earth Sci 24:1175-1184.

Dunning GR, Swinden HS, Kean BF, Evans DTW, Jenner GA (1991) A Cambrian island arc in Iapetus; geochronology and geochemistry of the Lake Ambrose volcanic belt, Newfoundland Appalachians. Geol Mag 128:1-17.

Elsgaard L, Isaksen MF, Jørgensen BB, Alayse A-M, Jannasch HW (1994) Microbial sulphate reduction in deep-sea sediments at the Guaymas Basin hydrothermal vent area: Influence of temperature and substrates. Geochimica et Cosmochimica Acta 58:3335-3343.

Evans DTW, Kean BF (2002) The Victoria Lake Supergroup, central Newfoundland - its definition, setting and volcanogenic massive sulphide mineralization.

Newfoundland and Labroador Department of Mines and Energy, Geological Survey, Open File NFLD/2790, pp 68.

Frank KL, Rogers DR, Olins HC, Vidoudez C, Girguis PR (2013) Characterizing the distribution and rates of microbial sulfate reduction at Middle Valley hydrothermal vents. International Society for Microbial Ecology 7:1391-1401.

Franklin JM, Sangster DM, Lydon JW (1981) Volcanic-associated massive sulphide deposits In: Skinner BJ (ed) Econ Geol Seventy-Fifth Anniversary Volume. Society of Economic Geologists, pp 485-627.

Franklin JM, Thorpe RI (1982) Comparative metallogeny of the Superior, Slave and Churchill provinces. Special Paper - Geological Association of Canada 25:3-90.

Franklin JM, Gibson HL, Galley AG, Jonasson IR (2005) Volcanogenic massive sulphide deposits In: Hedenquist JW, Thompson JFH, Goldfarb RJ, Richards JP (eds) Econ Geol 100th Anniversary Volume. Society of Economic Geologists, Littleton, CO, pp 523-560.

Fraser D, Giroux GA, Copeland DA, Devine CA (2012) NI-43-101 Technical Report and Mineral Resource Estimate on the Lemarchant Deposit, South Tally Pond VMS Project, central Newfoundland, Canada for Paragon Minerals Corporation. National Instrument 43-101 Technical Report, Toronto, ON, Canada, pp 137.

Füchtbauer H, Heling D, Müller G, Richter DK, Schmincke H-U, Schneider H-J, Valeton I, Walther HW, Wolf M (1988) Sedimente und Sedimentgesteine - Sedimentpetrologie, Teil II. Stuttgart. pp 1-1141.

Galley AG, Hannington M, Jonasson I (2007) Volcanogenic massive sulphide deposits In: Goodfellow WD (ed) Mineral Deposits of Canada: A Synthesis of Major Deposit-types, District Metallogeny, the Evolution of Geological Provinces, and Exploration Methods. Special Publication 5, Mineral Deposits Division, Geological Association of Canada, pp 141-161.

German CR, Von Damm KL (2003) Hydrothermal Processes  Treatise on Geochemistry. Pergamon, Oxford, pp 181-222.

Gill SB, Piercey SJ (2014) Preliminary mineralogy of barite-associated sulphide mineralization in the Ordovician Zn-Pb-Cu-Ag-Au Lemarchant volcanogenic massive sulphide deposit, Newfoundland and Labrador. Current Research - Geological Survey of Canada 2013-17:15. doi: 10.4095/292708.

Gill SB (2015) Mineralogy, metal zoning, and genesis of the Zn-Pb-Ba-Ag-Au Lemarchant volcanogenic massive sulphide (VMS) deposit. Master Thesis. Department of Earth Sciences. Memorial University of Newfoundland, St. John's.

Goodfellow WD, Peter JM (1996) Sulphur isotope composition of the Brunswick No. 12 massive sulphide deposit, Bathurst Mining Camp, New Brunswick: implications for ambient environment, sulphur source and ore genesis. Can J Earth Sci 33:231-251.

Gottschal JC, Prins RA (1991) Thermophiles: A life at elevated temperatures. Trends Ecol Evol 6:157-162.

Gundersen J, K., Jørgensen BB, Larsen E, Jannasch HW (1992) Mats of giant sulphur bacteria on deep-sea sediments due to fluctuating hydrothermal flow. Nature 360:454-456.

Gurvich EG (2006) Metalliferous sediments of the World Ocean - Fundamental theory of deep sea hydrothermal sedimentation. Springer Berlin Heidelberg. pp 1-416.

Habicht KS, Canfield DE (1997) Sulphur isotope fractionation during bacterial sulphate reduction in organic-rich sediments. Geochim Cosmochim AC 61:5351-5361.

Habicht KS, Canfield DE (2001) Isotope fractionation by sulphate-reducing natural populations and the isotopic composition of sulphide in marine sediments. Geol 29:555-558.

Hannington MD, Jonasson IR, Herzig PM, Petersen S (1995) Physical and chemical processes of seafloor mineralization at mid-ocean ridges In: Humphris SE, Zierenberg RA, mullineaux LS, Thomson RS (eds) Seafloor Hydrothermal Systems: Physical, Chemical, Biological and Geological Interactions. pp 115-157.

Hannington MD, Poulsen KH, Thompson JFH, Sillitoe RH (1999) Volcanogenic gold in the massive sulfide environment In: Barrie CT, Hannington MD (eds) Volcanic-Associated Massive Sulfide Deposits: Processes and Examples in Modern and Ancient Settings. Society of Economic Geologists, Littleton, CO, USA, pp 325-356.

Hannington MD (2009) Modern submarine hydrothermal systems - a global perspective on distribution, size, and tectonic settings In: Cousens BL, Piercey SJ (eds) Submarine Volcanism and Mineralization: Modern through Ancient. Geological Association of Canada, pp 91-148.

Hannington MD (2014) Volcanogenic massive sulphide deposits In: Holland HD, and Turekian, K.K. (ed) Treatise on Geochemistry 2nd Edition. Elsevier Ltd, pp 319-350.

Harazim D, Callow RHT, McIlroy D (2013) Microbial mats implicated in the generation of intrastratal shrinkage ('synaeresis') cracks. Sedimentology 6:1621-1638.

Harrison AG, Thode HG (1957) The kinetic isotope effect in the chemical reduction of sulphate. Trans Faraday Society 53:1648-1651.

Harrison AG, Thode HG (1958) Mechanism of the bacterial reduction of sulphate from isotope fractionation studies. Trans Faraday Soc 54:84-92.

Haymon RM, Kastner M (1981) Hot spring deposits on the East Pacific Rise at 21°N: preliminary description of mineralogy and genesis. Earth Planet Sci Lett 53:363-381. doi: 10.1016/0012-821x(81)90041-8.

Haymon RM, Fornari DJ, Von Damm KL, Lilley MD, Perfit MR, Edmond JM, Shanks Iii WC, Lutz RA, Grebmeier JM, Carbotte S, Wright D, McLaughlin E, Smith M, Beedle N, Olson E (1993) Volcanic eruption of the mid-ocean ridge along the East Pacific Rise crest at 9°45–52′N: Direct submersible observations of seafloor phenomena associated with an eruption event in April, 1991. Earth Planet Sci Lett 119:85-101. doi: http://dx.doi.org/10.1016/0012-821X(93)90008-W.

Hekinian R, Hoffert M, Larqué P, Cheminée JL, Stoffers P, Bideau D (1993) Hydrothermal Fe and Si oxyhydroxide deposits from South Pacific intraplate volcanoes and East Pacific Rise axial and off-axial regions. Econ Geol 88:2099-2121.

Hinchey JG, McNicoll V (2009) Tectonostratigraphic architecture and VMS mineralization of the southern Tulks Volcanic Belt: New insights from U-Pb geochronology and lithogeochemistry In: Pereira CPG, Walsh DG (eds) Current Research. Geological Survey Branch, St. John's, NL, Canada, pp 13-42.

Hodkinson RA, Cronan DS (1995) Hydrothermal sedimentation at ODP Sites 834 and 835 in relation to crustal evolution of the Lau backarck basin In: Parson LM,

Walker CL, Dixon DR (eds) Hydrothermal vents and processes. Geological Society Special Publication, pp 231-248.

Huston D, Relvas J, Gemmell J, Drieberg S (2011) The role of granites in volcanic-hosted massive sulphide ore-forming systems: an assessment of magmatic–hydrothermal contributions. Miner Deposita 46:473-507. doi: 10.1007/s00126-010-0322-7.

Huston DL (1999) Stable isotopes and their significance for understanding the genesis of volcanic-hosted massive sulphide deposits; a review. Rev Econ Geol 8:157-179.

Jørgensen BB (1990) A thiosulphate shunt in the sulphur cycle of marine sediments. Science 249:152-154.

Jørgensen BB, Isaksen MF, Jannasch HW (1992) Bacterial sulphate reduction above 100°C in deep-sea hydrothermal vent sediments. Science 258:1756-1757. doi: 10.1126/science.258.5089.1756.

Kalogeropoulos SI, Scott SD (1989) Mineralogy and geochemistry of an Archean tuffaceous exhalite; the Main Contact Tuff, Millenbach Mine area, Noranda, Quebec. Can J Earth Sci 26:88-105.

Kampschulte A, Strauss H (2004) The sulphur isotopic evolution of Phanerozoic seawater based on the analysis of structurally substituted sulphate in carbonates. Chem Geol 204:255-286. doi: http://dx.doi.org/10.1016/j.chemgeo.2003.11.013.

Kaplan IR, Rittenberg SC (1964) Microbiological Fractionation of sulphur isotopes. J Gen Microbiol 34:195-212.

Kemp ALW, Thode HG (1968) The mechanism of the bacterial reduction of sulphate and of sulphite from isotope fractionation studies. Geochim Cosmochim AC 32:71-91.

Konhauser KO (2007) Introduction to Geomicrobiology. Blackwell Publishing Ltd.

Kramers JD, Tolstikhin IN (1997) Two terrestrial lead isotope paradoxes, forward transport modelling, core formation and the history of the continental crust. Chem Geol 139:75-110. doi: http://dx.doi.org/10.1016/S0009-2541(97)00027-2.

Lode, S., Piercey, J. S., and Devine, C. A., 2015, Geology, Mineralogy, and Lithogeochemistry of Metalliferous Mudstones Associated with the Lemarchant Volcanogenic Massive Sulfide Deposit, Tally Pond Belt, Central Newfoundland: Economic Geology, v. 110, p. 1835-1859.

Lydon JW (1984) Ore deposit models; 8, Volcanogenic sulphide deposits; Part I, A descriptive model. Geosci Can 11:195-202.

McNicoll V, Squires G, Kerr A, Moore P (2010) The Duck Pond and Boundary Cu-Zn deposits, Newfoundland: new insights into the ages of host rocks and the timing of VHMS mineralization. Can J Earth Sci 47:1481-1506.

Mercier-Langevin P, Hannington M, Dubé B, Bécu V (2011) The gold content of volcanogenic massive sulfide deposits. Mineralium Deposita 46:509-539. doi: 10.1007/s00126-010-0300-0.

Mills RA, Elderfield H (1995) Hydrothermal activity and the geochemistry of metalliferous sediment. Geophysical Monograph 91:392-407.

Murowchick JB, Barnes HL (1986) Marcasite precipitation from hydrothermal solutions. Geochim Cosmochim AC 50:2615-2629.

Ohmoto H, Rye RO (1979) Isotopes of sulphur and carbon In: Barnes HL (ed) Geochemistry of Hydrothermal Ore Deposits, Second Edition. John Wiley & Sons : New York, NY, United States, United States, pp 509-567.

Ohmoto H, Goldhaber MB (1997) Sulphur and carbon isotopes In: Barnes HL (ed) Geochemistry of Hydrothermal Ore Deposits, Third Edition. John Wiley and Sons, pp 517-611.

Peter JM (2003) Ancient iron formations: their genesis and use in the exploration for stratiform base metal sulphide deposits, with examples from the Bathurst Mining Camp In: Lentz DR (ed) Geochemistry of Sediments and Sedimentary Rocks: Secular Evolutionary Considerations to Mineral Deposit-Forming Environments. Geological Association of Canada, pp 145-176.

Peter, JM, Goodfellow, WD (2003) Hydrothermal sedimentary rocks of the Heath Steele Belt, Bathurst mining camp, New Brunswick; Part 3, Application of mineralogy and mineral and bulk compositions to massive sulfide exploration: Economic Geology Monographs, pp 417-433.

Piercey SJ (2007) Volcanogenic massive sulphide (VMS) deposits of the Newfoundland Appalachians: An overview of their setting, classification, grade-tonnage data, and unresolved questions In: Pereira CPG, Walsh DG (eds) Current Research. Geological Survey Branch, St. John's, NL, pp 169-178.

Piercey SJ, Squires GC, Brace TD (2014) Lithostratigraphic, hydrothermal, and tectonic setting of the Boundary volcanogenic massive sulphide deposit, Newfoundland Appalachians, Canada: Formation by subseafloor replacement in a Cambrian Rifted Arc. Econ Geol 109:661-687. doi: 10.2113/econgeo.109.3.661.

Pollock JC, Wilton DHC (2001) Metallogenic studies of the Tally Pond Belt, Victoria Lake Group; trace-element geochemistry and lead-isotope data from the Exploits Subzone, Newfoundland. Report - Government of Newfoundland and Labrador Department of Mines and Energy, Geological Survey, Report: 2001-1, pp247-266, Mar 2001.

Ridler, R. H. (1971) Analysis of Archean volcanic basins in the Canadian Shield using the exhalite concept: Bulletin of the Canadian Institute of Mining and Metallurgy, v. 64.

Rogers N, van Staal CR, McNicoll V, Pollock J, Zagorevski A, Whalen J (2006) Neoproterozoic and Cambrian arc magmatism along the eastern margin of the Victoria Lake Supergroup: A remnant of Ganderian basement in central Newfoundland? Precambrian Res 147:320-341.

Rogers N, van Staal C, Zagorevski A, Skulski T, Piercey SJ, McNicoll V (2007) Timing and tectonic setting of volcanogenic massive sulphide bearing terranes within the Central Mobile Belt of the Canadian Appalachians In: Milkereit B (ed) Proceedings of Exploration 07: Fifth Decennial International Conference on Mineral Exploration. Toronto, ON, pp 1199-1205.

Rye RO (1993) The evolution of magmatic fluids in the epithermal environment; the stable isotope perspective. Economic Geology 88:733-752. doi: 10.2113/gsecongeo.88.3.733.

Sangster DF (1968) Relative sulphur isotope abundances of ancient seas and strata-bound sulphide deposits. Proceedings of the the Geological Association of Canada 19:79-91.

Schieber J (2011) Marcasite in black Shales-a mineral proxy for oxygenated bottom waters and intermittent oxidation of carbonaceous muds. J Sediment Res 81:447-458. doi: Doi 10.2110/Jsr.2011.41.

Schoonen MAA, Barnes HL (1991) Reactions forming pyrite and marcasite from solution: II. Via FeS precursors below 100°C. Geochim Cosmochim AC 55:1505-1514.

Seal RR, II, Alpers CN, Rye RO (2000) Stable isotope systematics of sulphate minerals. Rev Mineral Geochem 40:541-602. doi: 10.2138/rmg.2000.40.12.

Seal RR, II (2006) Sulphur isotope geochemistry of sulphide minerals. Rev Mineral Geochem 61:633-677. doi: 10.2138/rmg.2006.61.12.

Shanks WC, Bischoff JL, Rosenbauer RJ (1981) Seawater sulphate reduction and sulphur isotope fractionation in basaltic systems: Interaction of seawater with fayalite and magnetite at 200-350∞C. Geochim Cosmochim AC 45:1977-1995. doi: 10.1016/0016-7037(81)90054-5.

Shanks WC (2001) Stable isotopes in seafloor hydrothermal hystems: vent fluids, hydrothermal deposits, hydrothermal alteration, and microbial processes. Rev Mineral Geochem 43:469-525. doi: 10.2138/gsrmg.43.1.469.

Shanks WC (2014) 13.3 - Stable isotope geochemistry of mineral deposits In: Turekian HDHK (ed) Treatise on Geochemistry (Second Edition). Elsevier, Oxford, pp 59-85.

Shanks WC, III, Woodruff LG, Jilson GA, Jennings DS, Modene JS, Ryan BD (1987) Sulphur and lead isotope studies of stratiform Zn-Pb-Ag deposits, Anvil Range, Yukon; basinal brine exhalation and anoxic bottom-water mixing. Econ Geol and the Bulletin of the Society of Economic Geologists, May 82:600-634.

Sillitoe RH, Hannington MD, Thompson JFH (1996) High sulfidation deposits in the volcanogenic massive sulfide environment. Economic Geology 91:204-212.

Spry PG, Peter JM, Slack JF (2000) Meta-exhalites as exploration guides to ore In: Spry PG, Marshall B, Vokes FM (eds) Metamorphosed and metamorphogenic ore deposits. Society of Economic Geologists, Littleton, CO, pp 163-201.

Squires GC, MacKenzie AC, MacInnis D (1991) Geology and genesis of the Duck Pond volcanogenic massive sulphide deposit In: Swinden HS, Evans DTW, Kean BF (eds) Metallogenic Framework of Base and Precious Metal Deposits, Central and Western Newfoundland. Geological Survey of Canada, Ottawa, ON, Canada, pp 56-64.

Squires GC, Moore PJ (2004) Volcanogenic massive sulphide environments of the Tally Pond volcanics and adjacent area; geological, lithogeochemical and geochronological results In: Pereira CPG, Walsh DG, Kean BF (eds) Current Research. Geological Survey Branch, St. John's, NL, pp 63-91.

Squires GC, Hinchey JG (2006) Geology of the Tally Pond volcanic belt and adjacent areas (parts of NTS 12A/09 & 12A/10). Map 2006-01. Government of Newfoundland and Labrador, Department of Natural Resources, Geological Survey.

Swinden HS, Thorpe RI (1984) Variations in style of volcanism and massive sulphide deposition in Early to Middle Ordovician island-arc sequences of the Newfoundland Central Mobile Belt. Econ Geol 79:1596-1619.

Swinden HS (1988) Introduction to volcanogenic sulphide deposits in Newfoundland In: Swinden HS, Kean BF (eds) The volcanogenic sulphide districts of central Newfoundland. Geological Association of Canada, pp 1-26.

Swinden HS (1991) Paleotectonic settings of volcanogenic massive sulphide deposits in the Dunnage Zone, Newfoundland Appalachians. Canadian Institute of Mining and Metallurgy Bulletin 84:59-89.

Thode HG, Kleerekoper H, McElcheran D (1951) Isotope fractionation in the bacterial reduction of sulphate. Research 4:581-582.

Tivey MK (2007) Generation of seafloor hydrothermal vent fluids and associated mineral deposits Oceanogr 20:50-65.

Tosdal RM, Wooden JL, Bouse RM (1999) Pb isotopes, ore deposits, and metallogenic terranes. Rev Econ Geol 12:1-28.

van Staal CR (2007) Pre-Carboniferous tectonic evolution and metallogeny of the Canadian Appalachians In: Goodfellow WD (ed) Mineral Deposits of Canada: A Synthesis of Major Deposit-types, District Metallogeny, the Evolution of Geological Provinces, and Exploration Methods. Special Publication 5, Mineral Deposits Division, Geological Association of Canada, pp 793-818.

van Staal CR, Barr SM (2011) Lithospheric architecture and tectonic evolution of the Canadian Appalachians and associated Atlantic margin In: Percival JA, Cook FA, Clowes RM (eds) Chapter 2 Tectonic Styles in Canada: the LITHOPROBE Perspective. Geological Association of Canada, pp 3-55.

Von Damm KL (1990) Seafloor hydrothermal activity; black smoker chemistry and chimneys. Annual Review of Earth and Planetary Sciences 18:173-204.

Williams H (1979) Appalachian Orogen in Canada. Can J Earth Sci 16:792-807.

Williams H, Colman-Sadd SP, Swinden HS (1988) Tectonostratigraphic subdivisions of central Newfoundland. Current Research, Part B. Geological Survey of Canada, Ottawa, ON, Canada, pp 91-98.

Woodruff LG, Shanks WC (1988) Sulphur isotope study of chimney minerals and vent fluids from 21°N, East Pacific Rise: Hydrothermal sulphur sources and disequilibrium sulphate reduction. J Geophys Res: Solid Earth 93:4562-4572. doi: 10.1029/JB093iB05p04562.

Wortmann UG, Bernasconi SM, Böttcher ME (2001) Hypersulfidic deep biosphere indicates extreme sulfur isotope fractionation during single-step microbial sulfate reduction. Geology 29:647-650.

Zagorevski A, van Staal CR, McNicoll VJ (2007) Distinct Taconic, Salinic, and Acadian deformation along the Iapetus suture zone, Newfoundland Appalachians. Can J Earth Sci 44:1567-1585.

Zagorevski A, van Staal CR, Rogers N, McNicoll VJ, Pollock J (2010) Middle Cambrian to Ordovician arc-backarc development on the leading edge of Ganderia, Newfoundland Appalachians. Geological Society of America Memoirs 206:367-396. doi: 10.1130/2010.1206(16).

Zartman RE, Doe BR (1981) Plumbotectonics; the model. Tectonophysics 75:135-162.

**List of Figures**

**Figure 1**. A) Tectonostratigraphic assemblages with the main zones of the Newfoundland Appalachians (Avalon, Gander, Dunnage, and Humber zones) and VMS occurrences within the Notre Dame and Exploits subzones.

Notre Dame Subzone VMS: 1 – York Harbour; 2 – 8 - Baie Verte Belt Deposits; 9 – 12, 46 – Springdale Belt Deposits; 13 – 29 Buchans-Roberts Arm Deposits.

Exploits Subzone VMS: 30 – 37 - Tulks Belt Deposits; Tally Pond Belt Deposits: 39 – Lemarchant; 40 – Duck Pond; 41 – Boundary; 42 – 45 – Point Leamington Belt Deposits. Modified after (Swinden, 1991) and Piercey (2007). B) Geological map of the Tally Pond volcanic belt. The Tally Pond group comprises the Lemarchant deposit and the Duck Pond and Boundary mines. Modified from Copeland (2009) and Squires and Hinchey (2006).

**Figure 2**. Map of the massive sulphides of the Lemarchant Main, 24 Zone, and Northwest Zone. Massive sulphides are projected to the surface. Drill holes with exhalites are displayed as red circles, if logged, and as orange circle if not logged, because holes were either not accessible or not drilled yet during the field sessions. White circles display drill holes that do not contain exhalites. Half-coloured circles indicate that some of the listed holes have exhalites (modified from Canadian Zinc Corporation).

**Figure 3.** Section 101N, LM11-65. A) EMS-type mudstone. Photograph of core box 37, 157.4 - 161.6 m, rows 1-3 (I), which continue in (II). Sequence of exhalite (E1), massive sulphide (MS), massive sulphide+barite (MSB1), exhalite (E2), massive sulphide+barite (MSB2). B) Schematic description of A. C) Digitized version of an in detail logged drill hole section. Sequence of A and B represented by red square. Sequence includes finely

laminated to reworked, sulphide- and Ba-rich (pyrite, chalcopyrite, barite, celsian) exhalites (E1), which conformably overlie Fe-rich red massive sphalerite ore (MS). Fe-content decreases downhole, i.e., red sphalerite-dominated massive sulphides grade into orange to honeybrown-dominated sphalerite. Honeybrown sphalerite ore grades downhole into barite-rich massive sulphides (MSB1). The latter conformably overlies finely laminated to partly reworked, sulphide- and Ba-rich (pyrite, chalcopyrite, barite, celsian) exhalites (E2) that are intercalated with chert-apatite layers. These exhalites (II) conformably overlie barite-rich massive sulphides (MSB2).

**Figure 4.** Section 99+75N, LM13-78. A) FEM-type mudstone. Photograph of a section of core box rows of a sequence of felsic volcanic rocks (massive to brecciated rhyolite), which are conformably overlain by FEM-type exhalites. Exhalites are finely laminated to reworked, sulphide-rich (pyrite, pyrrhotite, minor chalcopyrite), and intercalated by a 8 cm thick mineralized micaceous tuff layer. Sulphides occur parallel to the lamination and in cross-cutting veins. The exhalites are conformably overlain by the hanging wall basalts. B) Schematic description of A. C - Digitized version of an in detail logged drill hole section. Sequence of A and B represented by red square.

**Figure 5.** Section 101+25N, LM13-79. A) IFE-type mudstone. Photograph of two core box rows of interflow exhalites occurring within hanging wall mafic volcanic rocks. Exhalites are sulphide-rich (fine-disseminated pyrite plus recrystallized pyrite), and intercalated by chert. B) Schematic description of A. C) Digitized version of an in detail logged drill hole section. Sequence of A and B represented by red square.

**Figure 6.** A) Section 101+25N, LM13-79, 181.9 m. EMS-type exhalite, sample CNF25069. Photograph of a finely laminated, which is cross-cut by veins with

polymetallic sulphides. B) Section 101N, LM11-65, 157.7 m. EMS-type exhalite, sample CNF30982. Photograph of a reworked finely laminated pyrite-chalcopyrite-rich exhalite. C) Section 108N, LM11-50, 114.6 m. FEM-type exhalite, sample CNF20927. Photograph of a carbonaceous finely laminated exhalite with a black chert-apatite nodule. Two ~1 mm thick bands contain pyrite tubes. D) Section 101+25N, LM13-79, 169.0 m. IFE-type exhalite, sample CNF25072. Photograph of a reworked, possibly bioturbated carbonaceous pyrite-rich interflow exhalite. E) Section 102+70N, LM11-52, 210.4 m. EMS-type exhalite, sample CNF20990. Photomicrograph (reflected light, RL) of a framboid-cluster. Pyrite framboids are overgrown by euhedral pyrite. Tan rims on framboids show 'hairy' texture, which may reflect fossilized bacterial or archaeal textures. F) Section 101N, LM11-65, 157.7 m. EMS-type exhalite, sample CNF30982. Photomicrograph (RL) of euhedral marcasite (Mrc) in massive pyrite (Py) associated with chalcopyrite (Ccp) and sulphur isotopic results of spot analyses on these mineral phases. G) Section 108N, LM11-50, 114.6 m. FEM-type exhalite, sample CNF20927. RL microscope image of microbial pyrite (Py) tubes and later stage euhedral pyrite, arsenopyrite (Apy), sphalerite (Sp), with chalcopyrite disease, and chalcopyrite (Ccp) and sulphur isotopic results of spot analyses. H) Section 103+25N, LM11-59, 194.2 m. FEM-type exhalite, sample CNF30998. Photomicrograph (RL) of euhedral and massive pyrite (Py) with galena (Gn) inclusions and associated interstitial chalcopyrite (Ccp) and pyrrhotite and sulphur isotopic results of spot analyses.

**Figure 7**. A) Section 101+25N, LM13-79, 186.6 m. EMS-type exhalite, sample CNF25071b. Photomicrograph (RL) of an in epoxy embedded rock chip (epoxy puck) with Pb-Zn-massive sulphides grading into a chalcopyrite-, sphalerite-, and pyrite-rich

exhalite. Contact is conformable, but reworked. Spot analyses of detailed S- and Pb-analyses are marked in red and blue, respectively. B) Section 101+25N, LM13-79, 186.6 m. EMS-type exhalite, sample CNF25071b. Detailed photomicrograph (RL) of Figure 7a with euhedral pyrite (Py), sphalerite (Sp) with chalcopyrite-disease, galena (Gn), and chalcopyrite (Ccp) S- and Pb-spot analyses. C) Section 105N, LM08-24ext, 432.8 m. EMS-type exhalite, sample CNF20983. Photomicrograph (RL) of a framboids-rich exhalite with a sulphide-rich vein parallel lamination. Vein sulphides consist of euhedral pyrite (Py), interstitial chalcopyrite (Ccp), and pyrrhotite (Po) and were analysed for S-isotopes. D) Section 100+50N, LM13-76, 163.8 m. FEM-type exhalite, sample CNF25062b. Photomicrograph (RL) microscope image of a framboid-rich exhalite with a sulphide-rich vein cross-cutting lamination. Vein sulphides consist of euhedral pyrite (Py), interstitial chalcopyrite (Ccp), and galena (Gn) and were analysed for S- and Pb-isotopes. E) Section 100+50N, LM13-77, 139.6 m. FEM-type exhalite, sample CNF25064. Photomicrograph (RL) microscope image of pyrrhotite (Po) associated with chalcopyrite (Ccp), galena (Gn), and electrum (El) and S- and Pb-spot analyses. F) Section 101N, LM07-13, 165.5 m. EMS-type exhalite, sample CNF30955. Scanning electron microscope (SEM) image in back-scattered electron (BSE) mode of a sulphide-rich and Ba-bearing exhalite with high precious-metal contents. Acanthite (Aca) is associated with euhedral pyrite (Py), chalcopyrite (Ccp), Fe-rich sphalerite (Fe-Sp), barite, and Fe-rich chlorite (Fe-Chl). G) and H) Section 101N, LM07-13, 165.5 m. EMS-type exhalite, sample CNF30955. Photomicrograph (transmitted light, TL, II nicols) and SEM-BSE image of a barite-(Brt)vein cross-cutting a celsian-(Cls)rich exhalite. Other mineral phases are pyrite (py), chalcopyrite (Ccp), quartz (Qz), and hyalophane (hyal).

**Figure 8.** Histogram for polymetallic sulphides (pyrite, pyrrhotite, arsenopyrite, chalcopyrite, and galena) hosted within the Lemarchant exhalites. $\delta^{34}S$ values range from -38.8‰ to +14.4‰ (n = 210). Bin width = 2‰.

**Figure 9.** Diagram showing the spatial distribution in respect to the mineralization of the Lemarchant Main and Northwest zones and the $\delta^{34}S$ values for A) euhedral and framboidal pyrite, marcasite, and other biogenic textures, B) pyrrhotite and arsenopyrite, and C) chalcopyrite and galena.

**Figure 10.** A) $\delta^{34}S$ data ranges of pyrite (Py) including marcasite, pyrrhotite (Po), arsenopyrite (Apy), chalcopyrite (Ccp), and galena (Gn) with distribution shape and 95$^{th}$ percentile (hatched line), as well as the average (solid line). Dotted areas indicate $\delta^{34}S$ values that have only biogenically-derived sulphur sources, based on two-component mixing modeling. Hatched areas display $\delta^{34}S$ ranges that have mixed sources. B) Represents diagram in Figure 10a subdivided into the three exhalite types: EMS, FEM, and IFE. EMS-type exhalites have more TSR-derived sulphur contribution than IFE-type exhalites. FEM-type show intermediate ranges.

**Figure 11.** A) $^{207}Pb/^{204}Pb$ versus $^{206}Pb/^{204}Pb$ space for *in situ* SIMS measurements on galena hosted in EMS- and FEM-type Lemarchant exhalites. Growth curves were modelled after data from Kramers and Tolstikhin (1997) representing the different reservoirs Old Upper Crust, Average Crust, Young Upper Crust, and Mantle. The trendlines are York regressions and error ellipses are calculated using Isoplot 3.75. B) $^{208}Pb/^{204}Pb$ versus $^{206}Pb/^{204}Pb$ space.

**Figure 12.** $^{206}Pb/^{204}Pb$, $^{207}Pb/^{204}Pb$, and $^{208}Pb/^{204}Pb$ versus $\delta^{34}S$ for analyses on the same galena of the EMS- and FEM-type exhalites.

**Figure 13**. Modelled range of sulphur isotopes for sulphides with TSR-derived sulphur at 250°C, 300°C, and 350°C for A) pyrite, B) pyrrhotite, C) chalcopyrite, and D) galena, and the range of $\delta^{34}S$ values for the Lemarchant exhalite sulphides.

**Figure 14.** Mixing models between TSR- and BSR-derived sulphur for the sulphides: A) pyrite, B) pyrrhotite, C) chalcopyrite, and D) galena. The mixing lines are calculated based on BSR-derived $H_2S$ at each T = 0°C, 50°C, 100°C, and 120°C, with BSR-$H_2S$ at T = 300°C. The interception of the range of $\delta^{34}S$ values for each sulphide measured in this study (highlighted in its respective colour) and the BSR-TSR mixing lines are highlighted in hatched fields and represent the proportion of TSR-derived sulphur in the sulphides.

**Figure 15**. Pathway of sulphur isotopic composition explaining the large fractionation factors present in hydrothermal sedimentary sulphides. Initial sulphate reduction, either inorganic or organic, is followed by an intermediate step of microbial sulphide oxidation and followed by microbial disproportionation of sulphur intermediate compounds (thiosulphate, sulphite, and elemental sulphur) represented by $S_0$. Modified after Canfield (2001b).

**Figure 16**. Polymetallic sulphides in the Lemarchant exhalites have organic and inorganic sulphur sources. Inorganic sulphur sources are more prominent in euhedral pyrite, chalcopyrite, and galena hosted in exhalites proximal to vent (and massive sulphide mineralization) than in more distally precipitates ones. TSR = Thermochemical sulphate reduction, BSR = biogenic/microbial sulphate reduction, BSO = biogenic sulphide oxidation. A) A synvolcanic intrusion (possibly Lemarchant microgranite) provides the heat to drive hydrothermal circulation, and possibly adds magmatic/epithermal fluids and volatiles to seawater-derived hydrothermal fluid cells.

Hot hydrothermal fluids are focused along synvolcanic faults and discharged via black and white smoker into the ambient seawater. B) Close-up of exhalites with microbial mats on rock-water-interface (green rectangle). Exhalites with microbial mats are deposited around the vent site and form a semi-permeable cover layer. Hot hydrothermal fluids circulate upwards through semi-permeable exhalites and exit via diffuse venting onto the seafloor. The hydrothermal fluids mix with cold seawater within the sediment and after emanating. Thermophile and hyperthermophile bacteria and archaea (sulphide-oxidizing and sulphate-reducing) form laminae of microbial mats. Modified after Gundersen et al. (1992).

**Electronic Supplementary Material 4:**

**Figure** A) Section 104+51N, LM08-19, 98.9 m. EMS-type exhalite, sample CNF30957. Core-photograph of a sulphide-rich, partially reworked exhalite that is conformably overlain by a chert-jasper layer. B) Photomicrograph (TL, II nicols) of the contact between the exhalite and jasper, which is marked by stromatolite-like bulbous layers in finely laminated mudstone and chert layer of suggested microbial mats.

**List of Tables**

**ESM2.** Sulphur isotope data for pyrite, chalcopyrite, pyrrhotite, arsenopyrite, and galena hosted in the Lemarchant exhalites.

**ESM3.** Lead isotope data for galena hosted in the Lemarchant exhalites.

Figure 1a-b

# Fig. 1a-b

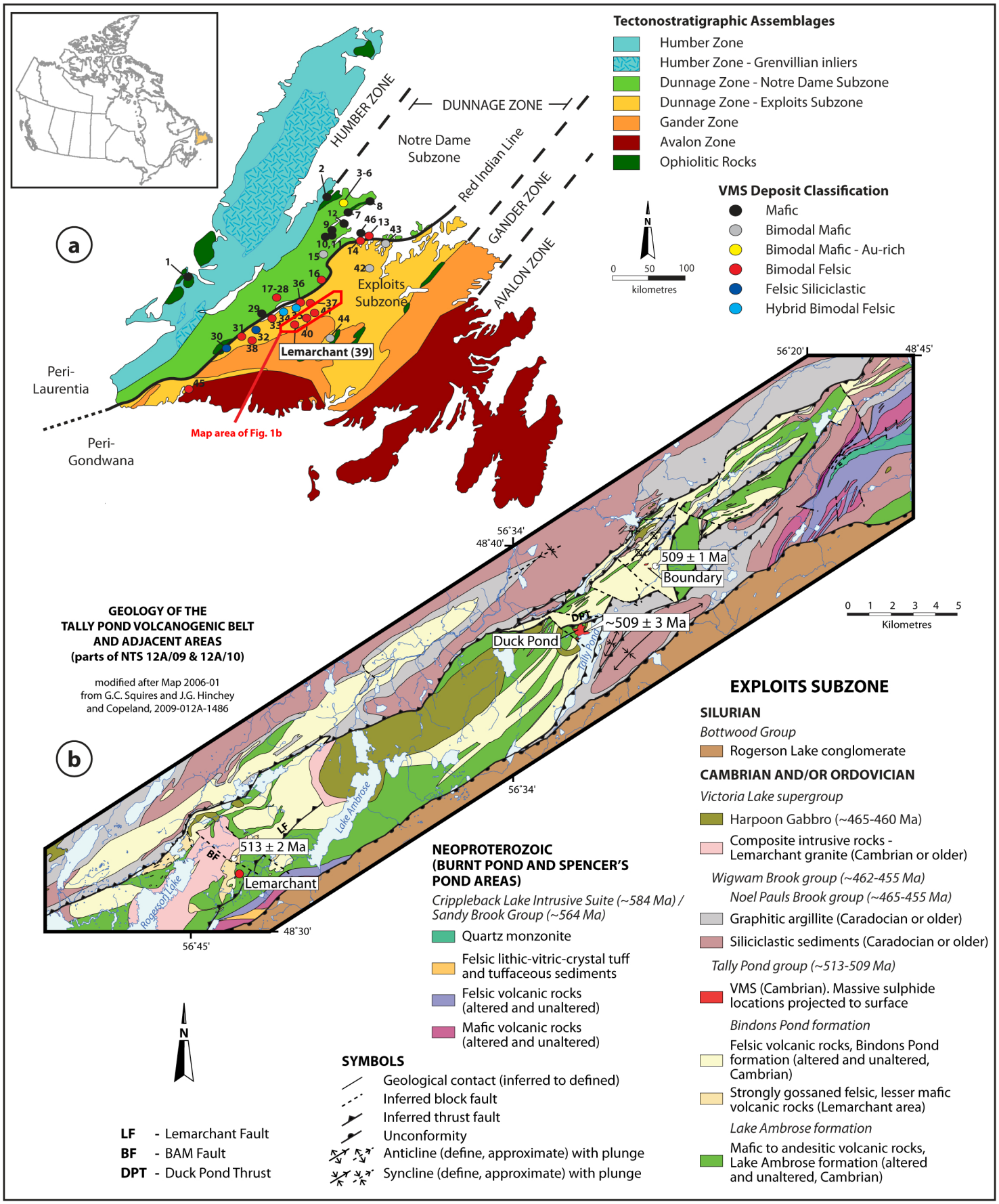

Figure 2

**Fig. 2**

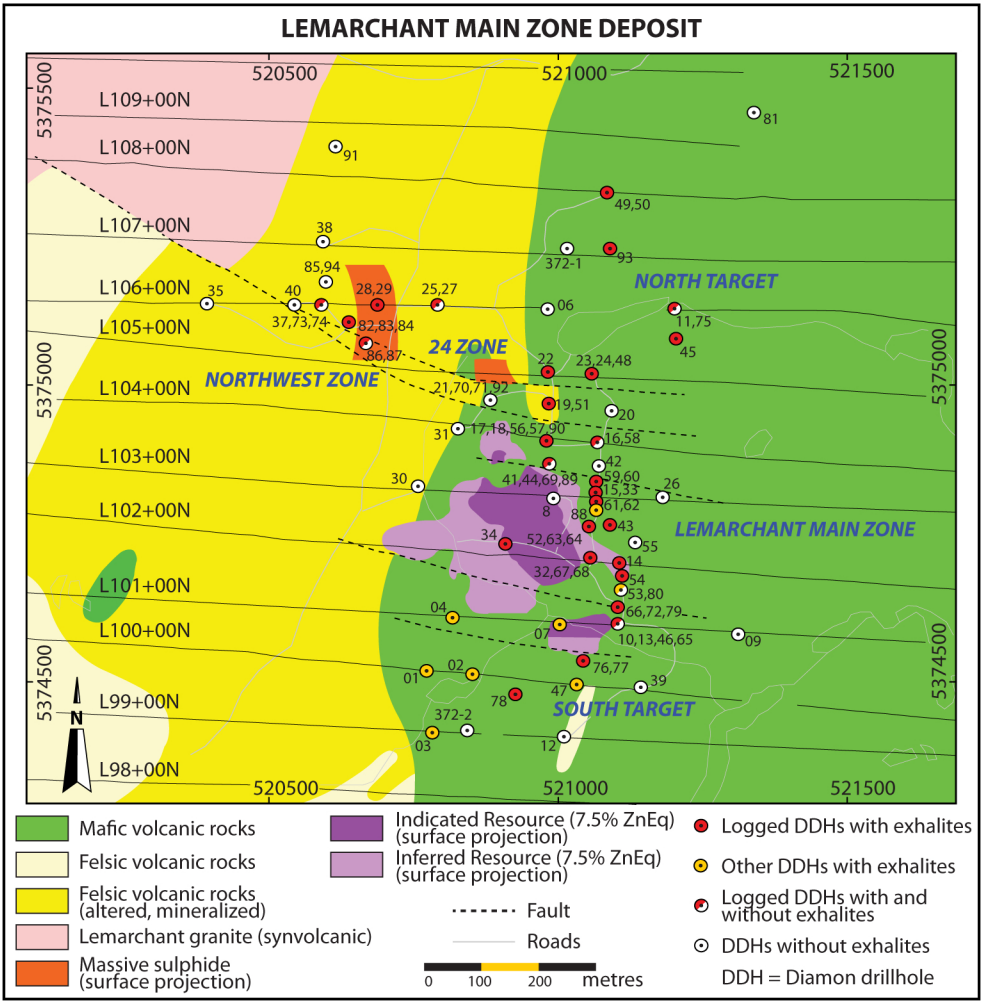

Figure 3 a-c

# Fig. 3a-c

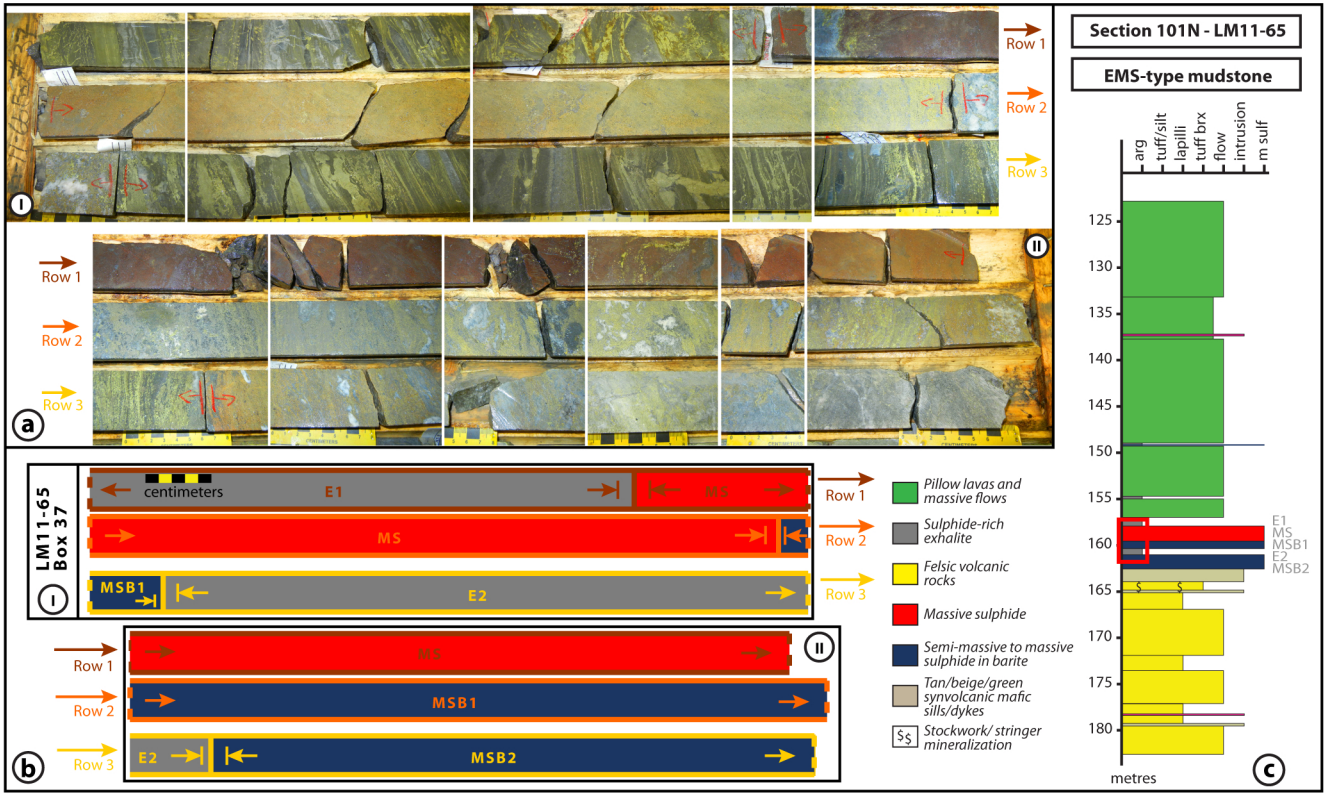

Figure 4a-c

**Fig. 4a-c**

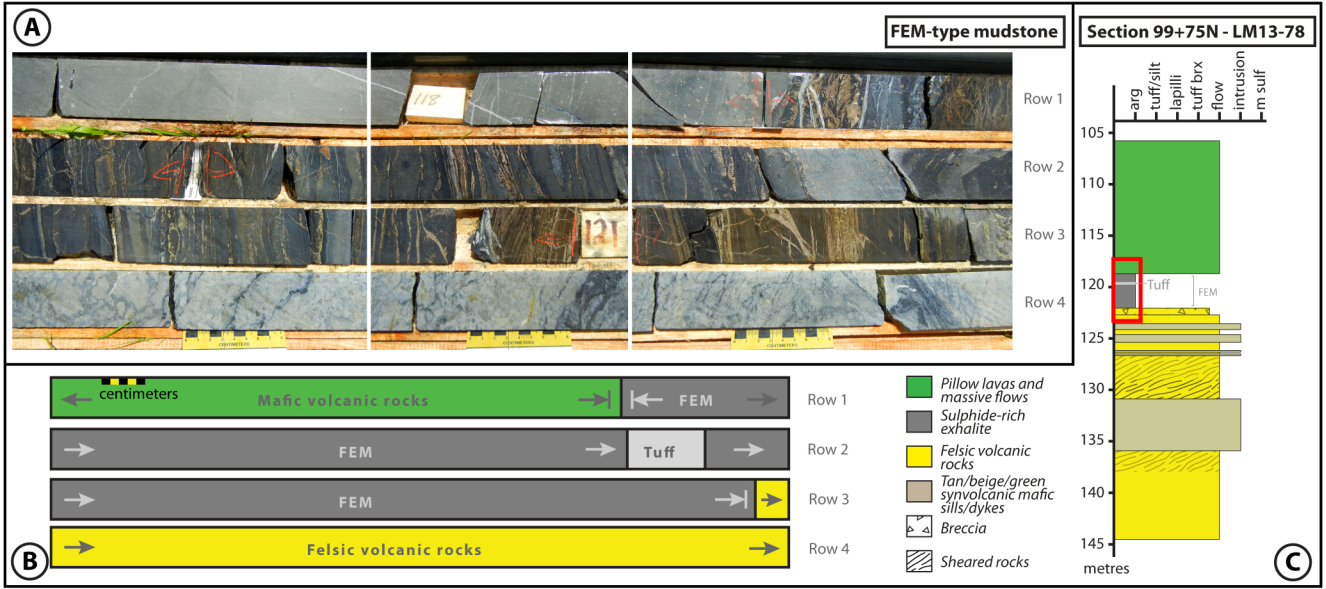

Figure 5a-c

**Fig. 5a-c**

Figure 6 a-h

# Fig. 6a-h

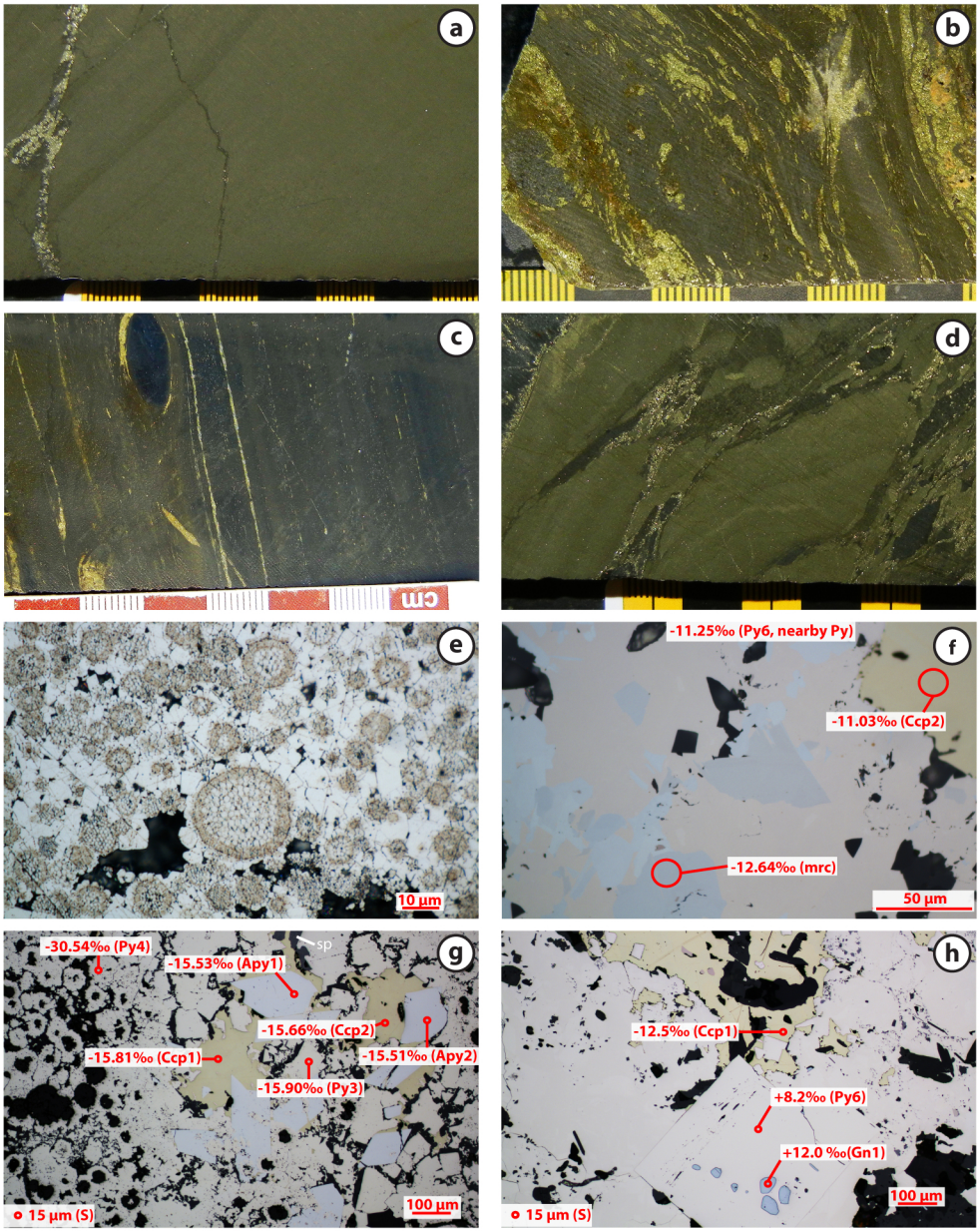

Figure 7a-h

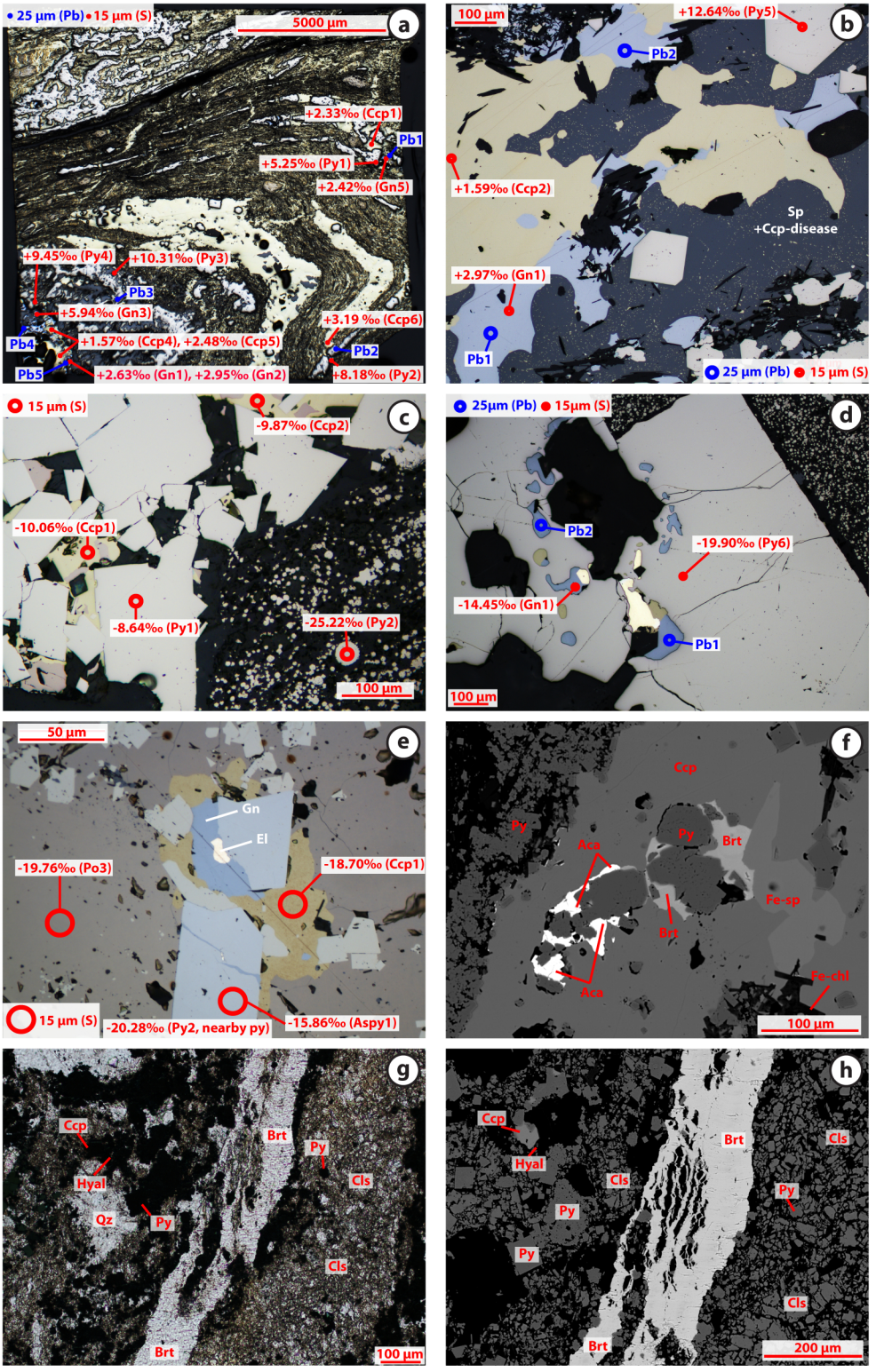
a
25 µm (Pb)
15 µm (S)
5000 µm
+2.33‰ (Ccp1)
Pb1
+5.25‰ (Py1)
+2.42‰ (Gn5)
+9.45‰ (Py4)
+10.31‰ (Py3)
Pb3
+5.94‰ (Gn3)
Pb4
+1.57‰ (Ccp4), +2.48‰ (Ccp5)
+3.19 ‰ (Ccp6)
Pb2
Pb5
+2.63‰ (Gn1), +2.95‰ (Gn2)
+8.18‰ (Py2)
b
100 µm
+12.64‰ (Py5)
Pb2
+1.59‰ (Ccp2)
Sp
+Ccp-disease
+2.97‰ (Gn1)
Pb1
25 µm (Pb)
15 µm (S)
c
15 µm (S)
-9.87‰ (Ccp2)
-10.06‰ (Ccp1)
-8.64‰ (Py1)
-25.22‰ (Py2)
100 µm
d
25µm (Pb)
15µm (S)
Pb2
-19.90‰ (Py6)
-14.45‰ (Gn1)
Pb1
100 µm
e
50 µm
Gn
El
-19.76‰ (Po3)
-18.70‰ (Ccp1)
15 µm (S)
-20.28‰ (Py2, nearby py)
-15.86‰ (Aspy1)
f
Ccp
Py
Py
Brt
Aca
Fe-sp
Brt
Aca
Fe-chl
100 µm
g
Ccp
Brt
Py
Hyal
Cls
Qz
Py
Cls
Brt
100 µm
h
Ccp
Brt
Cls
Hyal
Cls
Py
Py
Py
Cls
Brt
200 µm

Fig. 8

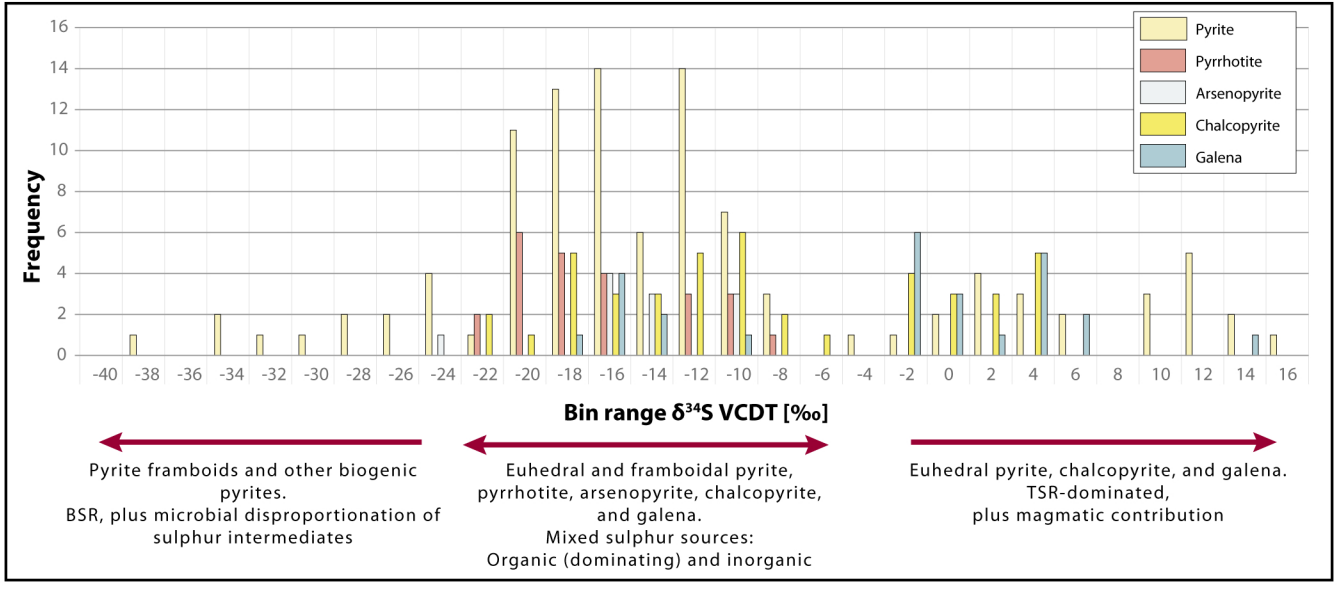
Pyrite
Pyrrhotite
Arsenopyrite
Chalcopyrite
Galena
Frequency
0
2
4
6
8
10
12
14
16
-40 -38 -36 -34 -32 -30 -28 -26 -24 -22 -20 -18 -16 -14 -12 -10 -8 -6 -4 -2 0 2 4 6 8 10 12 14 16
Bin range δ34S VCDT [‰]
Pyrite framboids and other biogenic pyrites.
BSR, plus microbial disproportionation of sulphur intermediates
Euhedral and framboidal pyrite, pyrrhotite, arsenopyrite, chalcopyrite, and galena.
Mixed sulphur sources:
Organic (dominating) and inorganic
Euhedral pyrite, chalcopyrite, and galena.
TSR-dominated,
plus magmatic contribution

Figure 9 a-c

# Fig. 9a-c

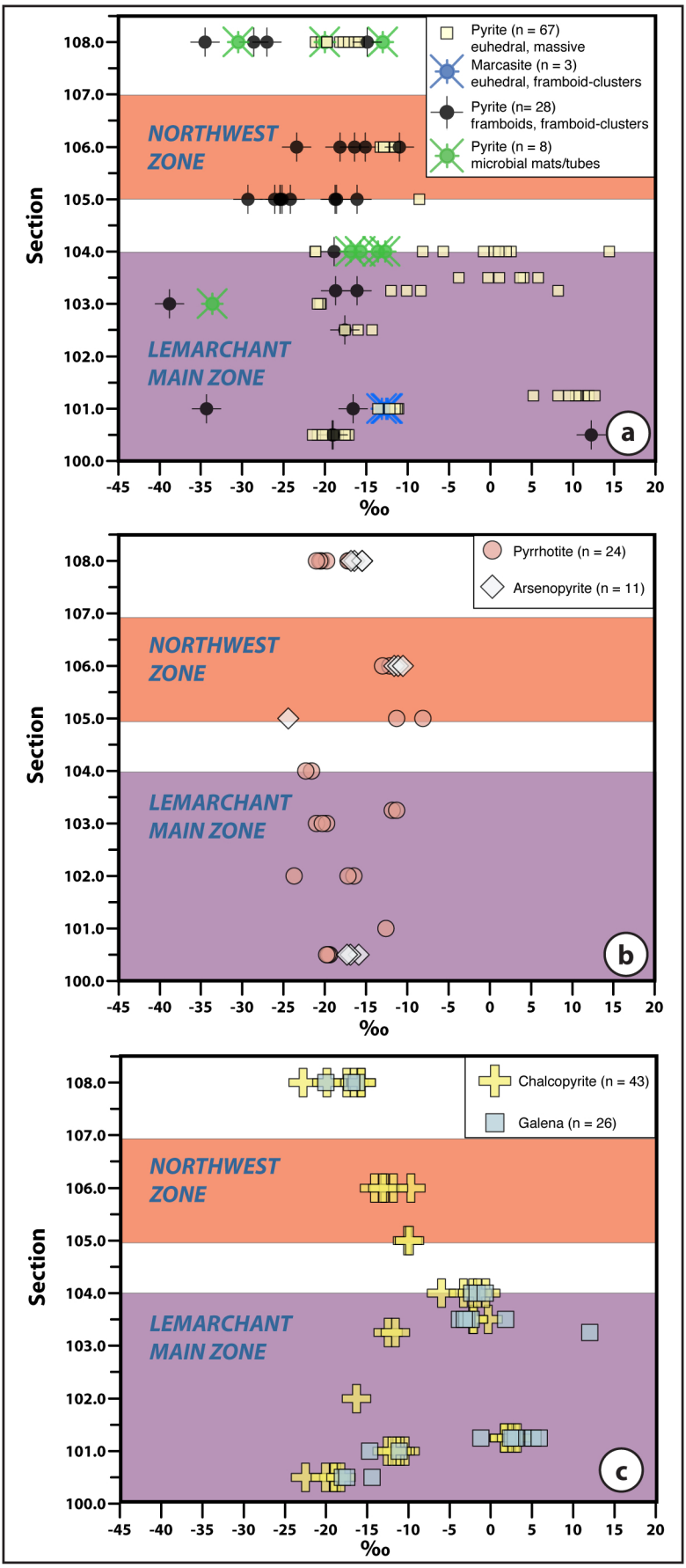

Figure 10 a-b

**Fig. 10a-b**

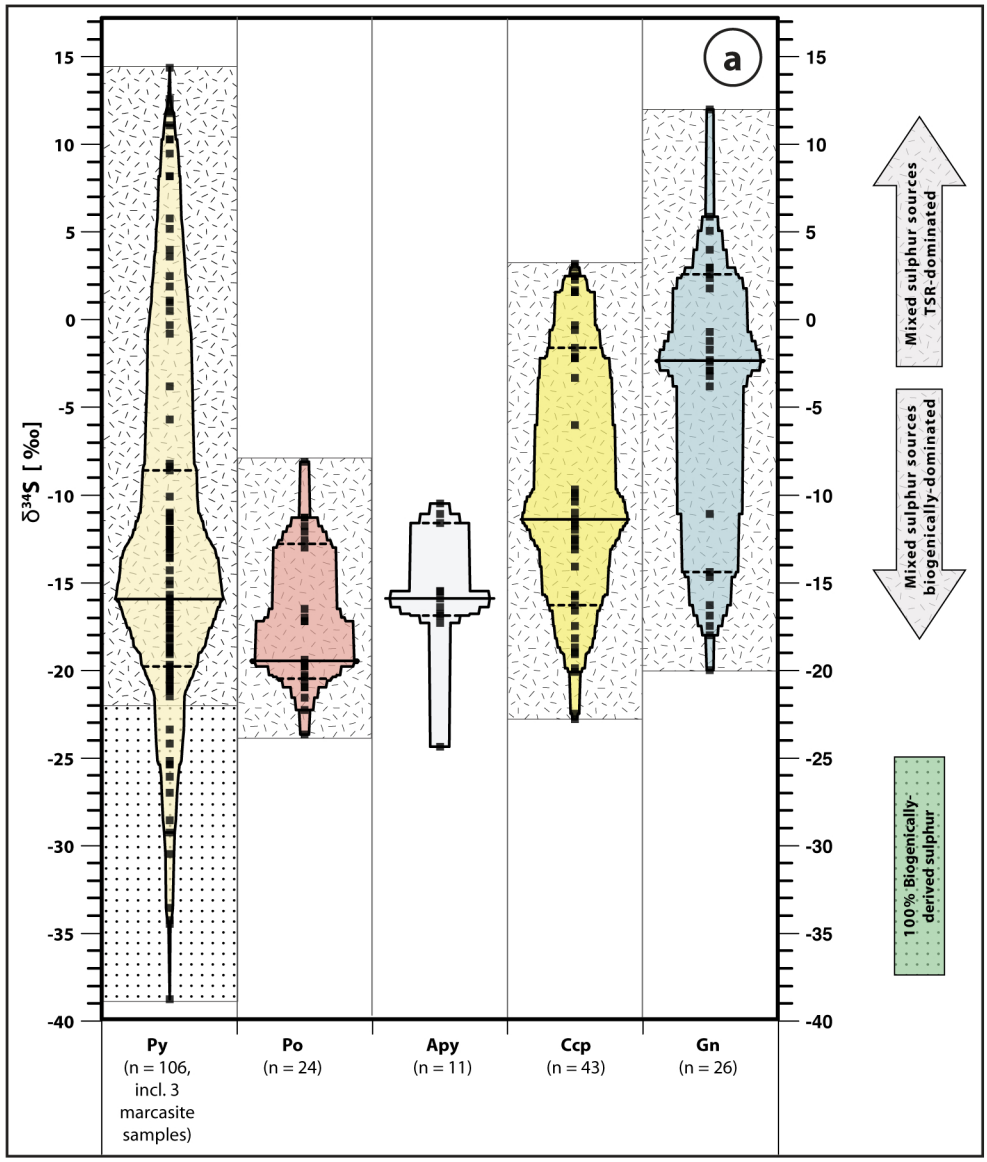


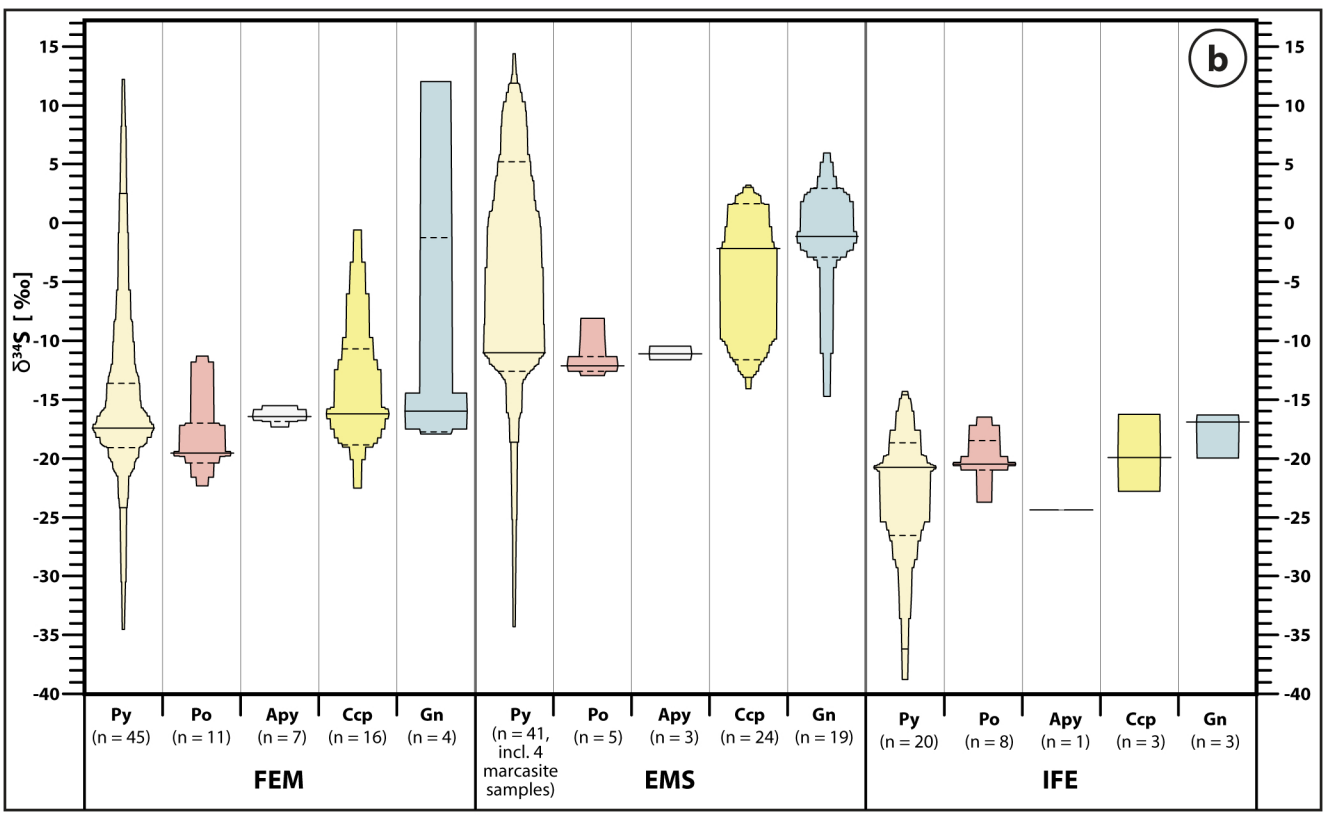

Figure 11 a-b

**Fig. 11a-b**

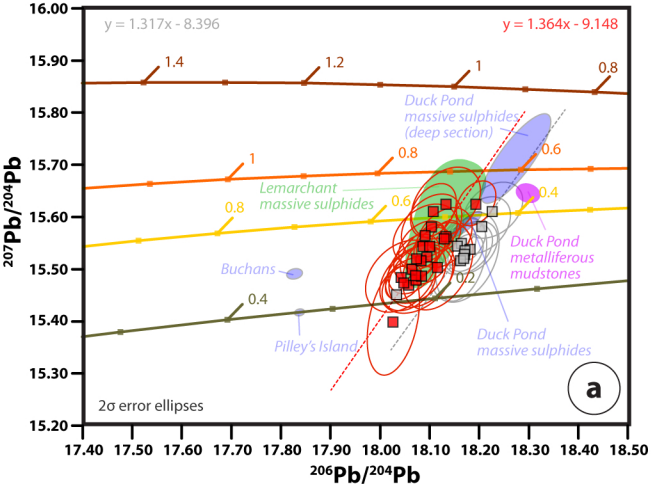


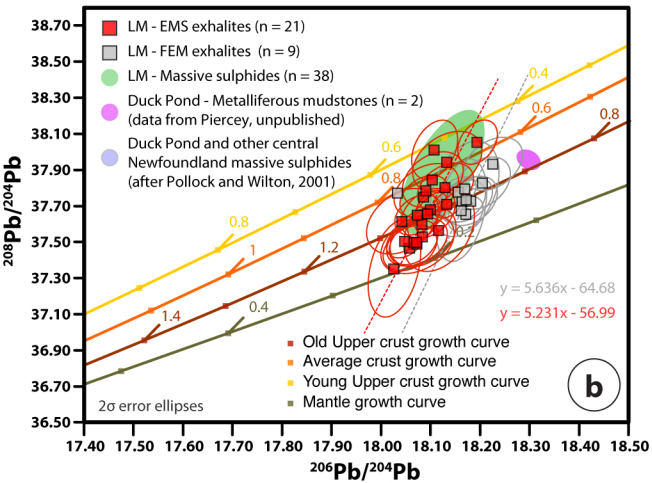

Figure 12a-c

# Fig. 12a-c

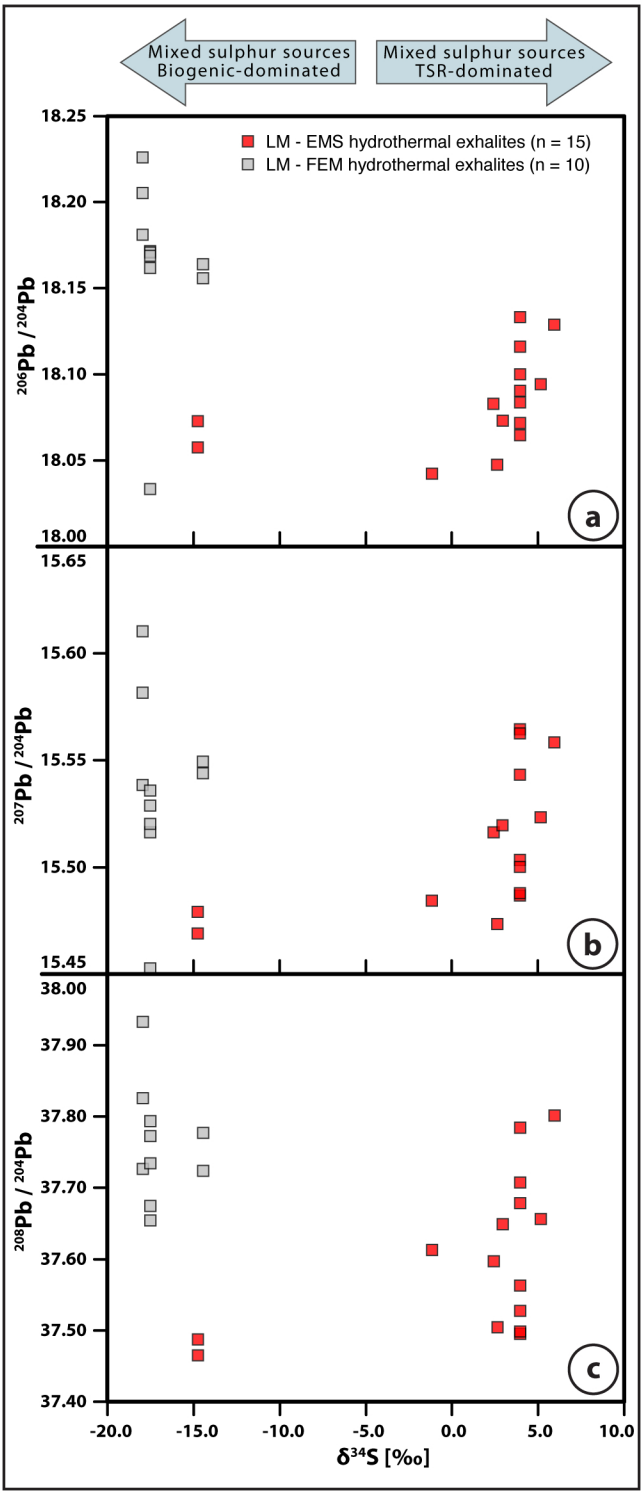

Figure 13 a-d

# Fig. 13a-d

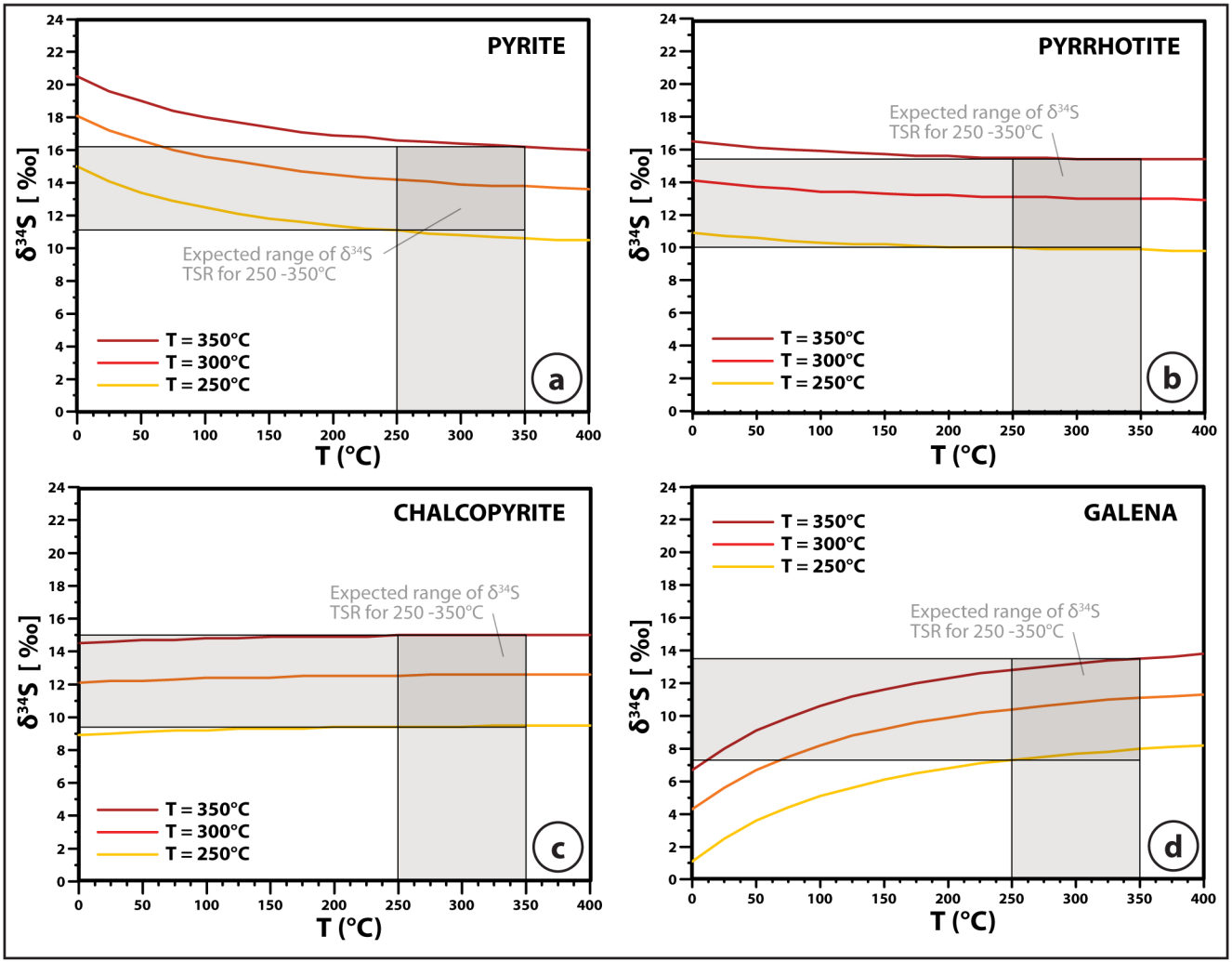

Figure 14 a-d

**Fig. 14a-d**

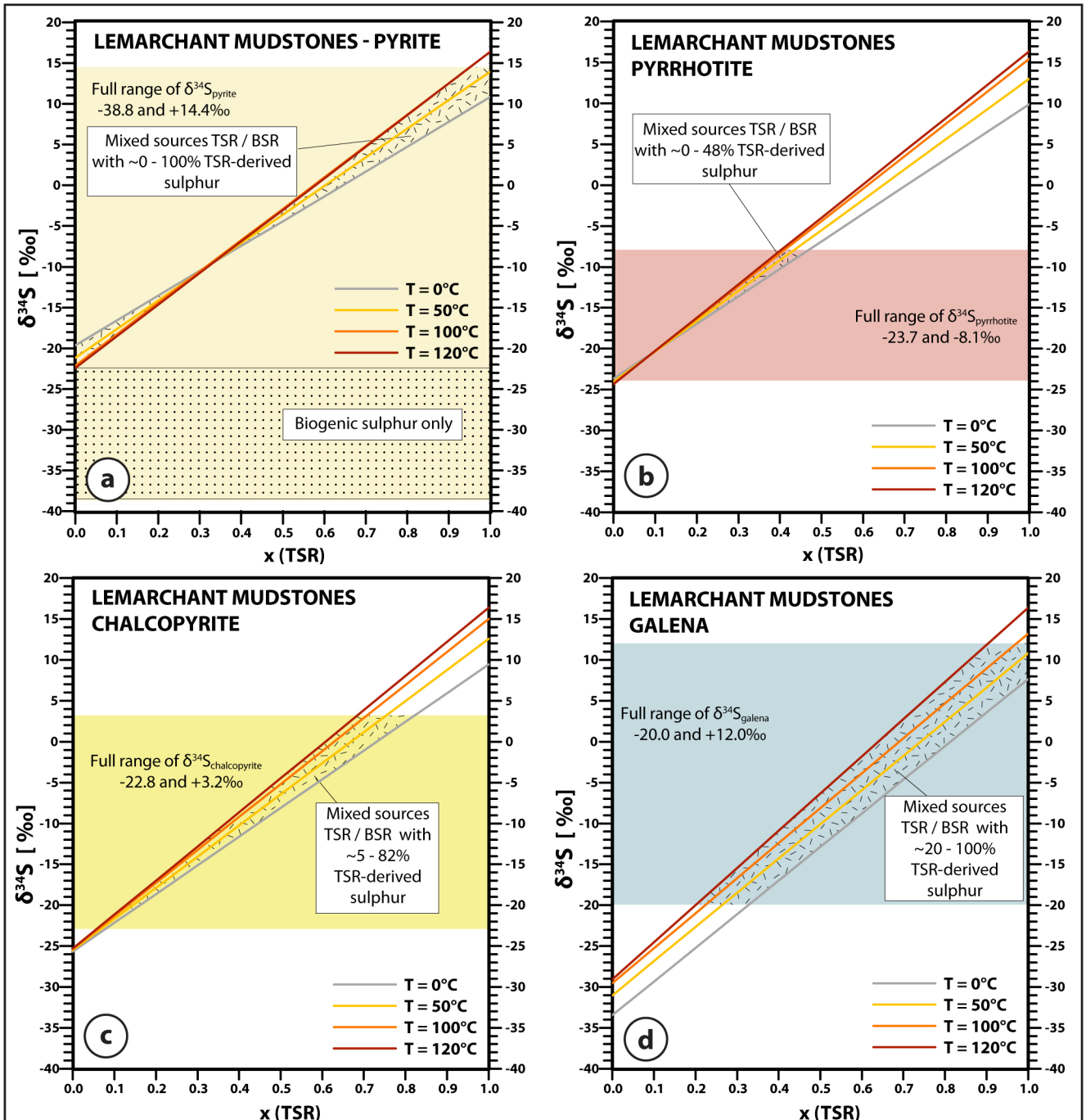

Figure 15

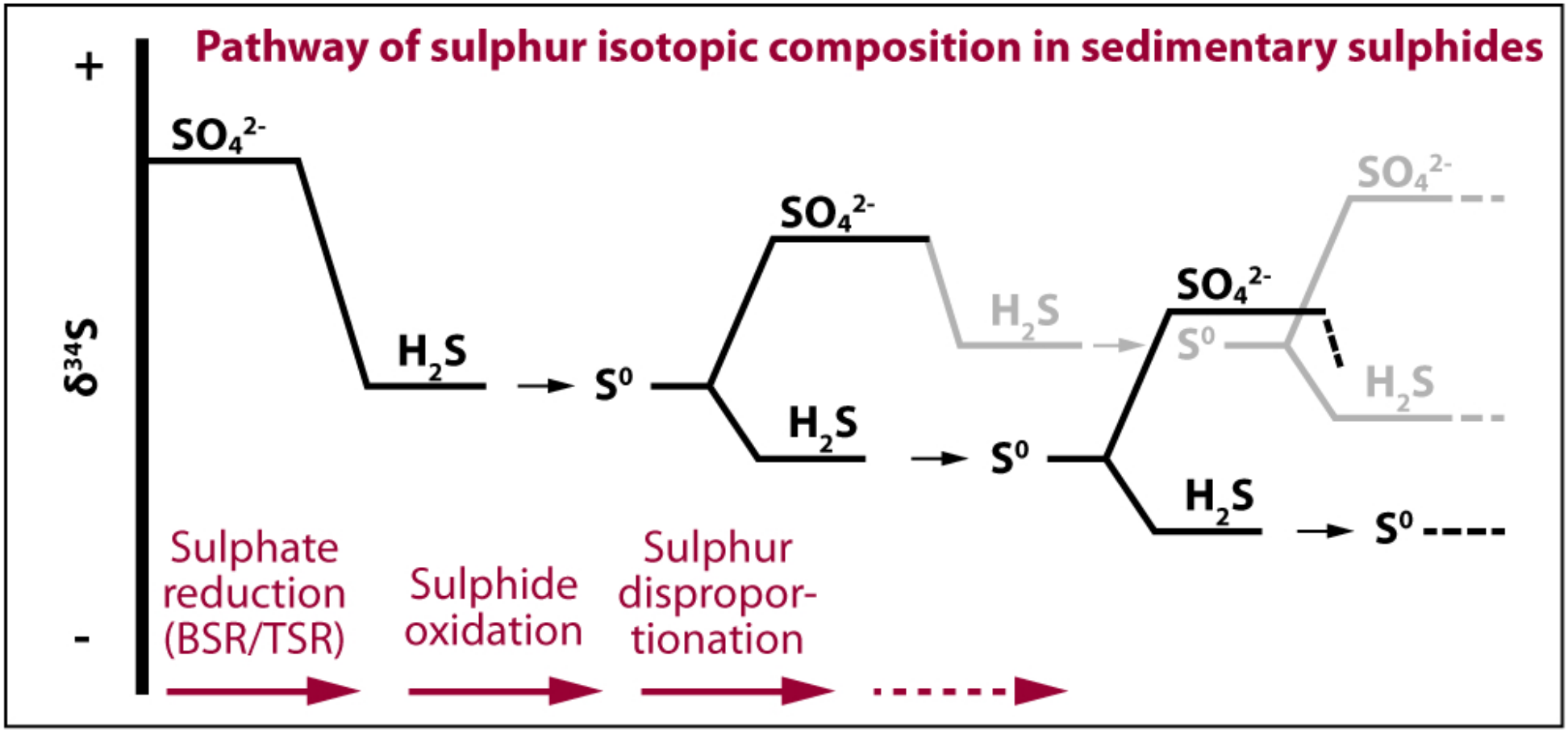
Pathway of sulphur isotopic composition in sedimentary sulphides
+
-
δ34S
SO42-
H2S
S0
SO42-
H2S
S0
H2S
SO42-
S0
H2S
SO42-
H2S
S0
Sulphate reduction (BSR/TSR)
Sulphide oxidation
Sulphur disproportionation

Figure 16 a-b

**Fig. 16a-b**

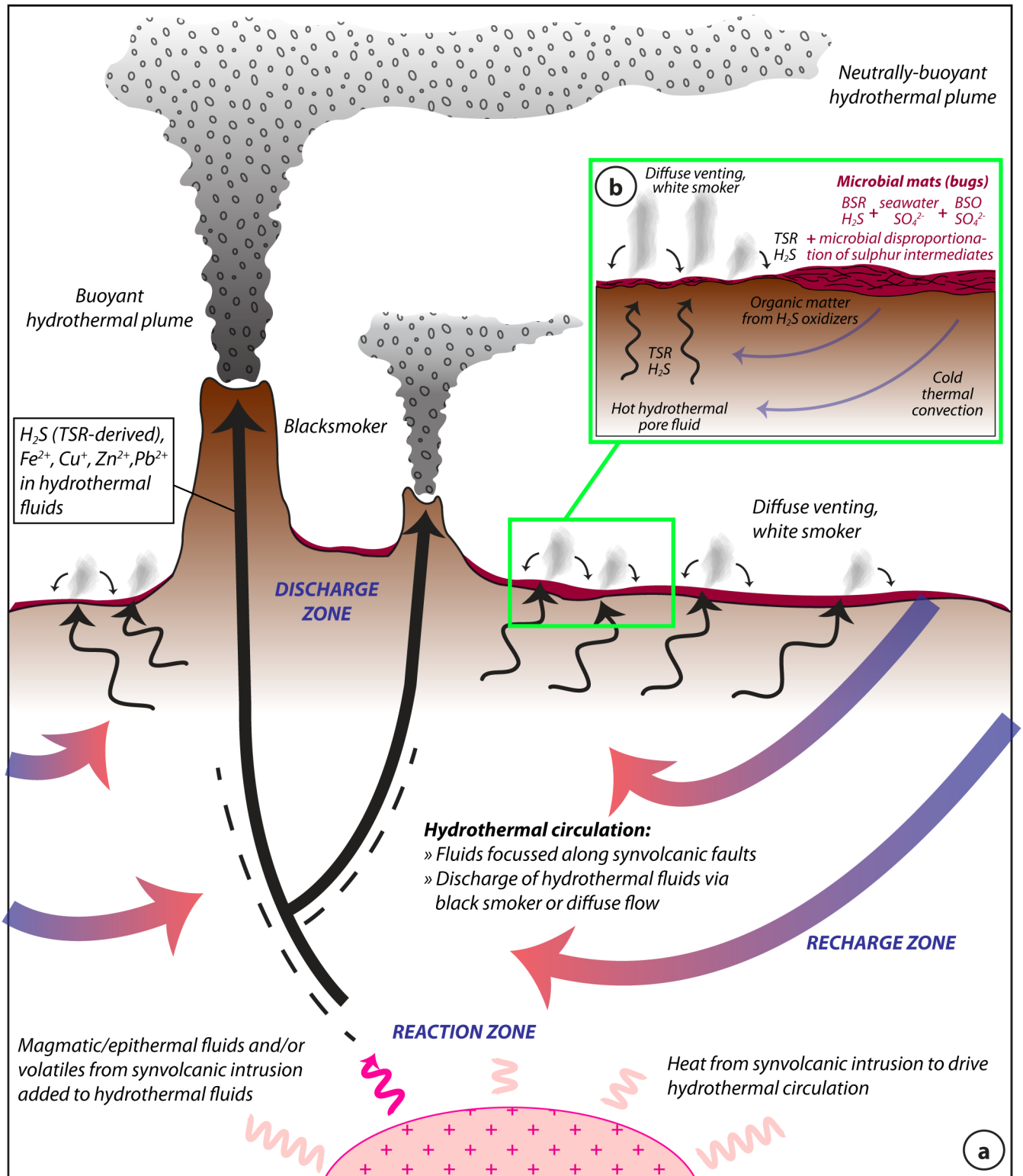


**Sulphur sources in metalliferous mudstones:**

**Inorganic**
1. $H_2S$ (TSR-derived)
2. $H_2S$ and sulphate from magmatic disproportionation of $SO_2$
3. Leaching of sulphur/sulphides from volcanic host rocks

**Organic**
4. $H_2S$ from bacterial sulphate reduciton (BSR)
5. $SO_4^{2-}$ from bacterial sulphide oxidation (BSO)
6. $H_2S$ and $SO_4^{2-}$ from microbial disproportionation of intermediate sulphur compounds (elemental sulphur, thiosulphate, sulphite)